



# Zonal Current Characteristics in the Southeastern Tropical Indian Ocean (SETIO)

Nining Sari Ningsih<sup>1</sup>, Sholihati Lathifa Sakina<sup>2</sup>, Raden Dwi Susanto<sup>3,2</sup>, Farrah Hanifah<sup>1</sup>

<sup>1</sup>Research Group of Oceanography, Faculty of Earth Sciences and Technology, Bandung Institute of Technology, Indonesia

5 <sup>2</sup>Department of Oceanography, Faculty of Earth Sciences and Technology, Bandung Institute of Technology, Indonesia

<sup>3</sup>Department of Atmospheric & Oceanic Science, University of Maryland, USA

*Correspondence to:* Nining Sari Ningsih (nining@fitb.itb.ac.id)

**Abstract.** Zonal current characteristics in the Southeastern Tropical Indian Ocean (SETIO) adjacent to the southern Sumatra-  
10 Java coasts have been studied using 64 years (1950-2013) data derived from simulated results of a 1/8° global version of the  
HYbrid Coordinate Ocean Model (HYCOM). This study has revealed distinctive features of zonal currents in the South Java  
Current (SJC) region, the Indonesian Throughflow (ITF)/South Equatorial Current (SEC) region, and the transition zone  
between the SJC and ITF/SEC regions. Empirical orthogonal function (EOF) analysis is applied to investigate explained  
variance of the current data and give results for almost 95-98% of total variance. The first temporal mode of EOF is then  
15 investigated by using ensemble empirical mode decomposition (EEMD) for distinguishing the signals. The EEMD analysis  
shows that zonal currents in the SETIO vary considerably from intraseasonal to interannual timescales. In the SJC region, the  
zonal currents are consecutively dominated by semiannual (0.140 power/year), intraseasonal (0.070 power/year), and annual  
(0.038 power/year) signals, while semiannual (0.135 power/year) and intraseasonal (0.033 power/year) signals with  
pronounced interannual variations (0.012 power/year) of current appear consecutively to be dominant modes of variability in  
20 the transition zone between the SJC and ITF/SEC regions. In contrast, there exist dominant interannual signal (0.017  
power/year) with prominent intraseasonal variability (0.012 power/year) of the current in the ITF/SEC region. In response to  
El Niño–Southern Oscillation (ENSO) event, El Niño (La Niña) events are favourable for an eastward (westward) zonal  
current. Meanwhile, an eastward (westward) anomaly of the current exists during negative (positive) Indian Ocean Dipole  
(IOD), which is associated with the presence of anomalous surface winds over the study area during those events. This work  
25 may contribute to further understanding of the variability of zonal current characteristics in the SETIO both in space and time  
as well as identification of its dominant time scales.

## 1 Introduction

Southeastern tropical Indian Ocean (SETIO) plays an important role in ocean and atmosphere dynamics of Indian Ocean.  
30 Several features make the SETIO region unique. This is partly due to the presence of the Indonesian Throughflow (ITF)



(Gordon, 1986; Wyrki, 1987; Murray and Arief 1988; and references hereafter), which transfers warm and fresh Pacific waters to the Indian Ocean and contributes to variability of sea surface temperature (SST) in the SETIO, particularly that in the area off Java and Sumatra, which in turn affects the climate system both at regional and global scales (Clark et al., 2003; Saji and Yamagata, 2003). In the SETIO, the complex dynamical circulations exist due to the coexistence of South Java Current (SJC),  
35 South Java Undercurrent (SJUC), South Equatorial Current (SEC), and also the ITF originating from the outflow passages (e.g., Sunda, Lombok, and Ombai Straits, and Timor Passage) and their mutual interactions. It has been recognized that the SJC and SJUC play an important role in distributing warm and fresh water into and out of the southeast Indian Ocean and in turn influencing the global climate system (e.g., Fieux et al., 1994, 1996; Sprintall et al., 1999, 2010; Wijffels et al., 2002; Wijffels and Meyers, 2004).

40 Previous studies have suggested that the current dynamics in the SETIO as well as ocean circulations in the inner Indonesian seas are strongly linked to the regional Indo-Pacific and global climates from intraseasonal, seasonal, interannual, and even longer timescales (e.g., Sprintall et al., 1999; Song et al., 2004; Iskandar et al., 2006; Yuan et al., 2008; Syamsudin and Kaneko, 2013; Sprintall and Révelard, 2014; Krishnamurthy and Krishnamurthy, 2016; Susanto et al., 2016). Thus, it is important to obtain a better understanding of current characteristics as well as their variations in the SETIO adjacent to the southern coasts  
45 of Sumatra and Java both for scientific and practical reasons, such as fisheries, climate, and navigation.

Several studies of seasonal variability of SJC and its deeper undercurrent (SJUC) those exist along the coasts of western Sumatra and southern Java have been carried out by previous investigators based on observation data (e.g., Sprintall et al., 1999; 2010; Qu and Meyers, 2005). In general, their studies have revealed that the SJC is eastward during the northwest (NW) monsoon (December to February; DJF) and the eastward-flowing SJC is enhanced in the presence of semiannual coastal Kelvin  
50 waves originating in the *equatorial Indian Ocean* during the first (March to May; MAM) and second (September to November; SON) transitional monsoons. During the southeast (SE) monsoon (July to August; JJA), the SJC flows mostly westward. Moreover, Sprintall et al., (2010) have confirmed the extension of SJC and SJUC into Ombai Strait through Sawu Sea based on 3-year velocity measurements (2004–2006).

In addition, Iskandar et al. (2006) have confirmed the existence of intraseasonal variations of SJC and SJUC of the southern  
55 Sumatra-Java coasts using simulated data from an ocean general circulation model (OGCM) for 13 years (1990–2003). They found that the intraseasonal SJC is dominated by the 90-day variations associated with propagation of the first baroclinic Kelvin waves, which are driven by strong 90-day winds over the central equatorial Indian Ocean. Meanwhile, 60-day variations are the dominant feature in the SJUC, which are forced by intraseasonal atmospheric variability associated with the eastward movement of the Madden-Julian Oscillation (MJO) over the eastern equatorial Indian Ocean.

60 Moreover, like SJC, ITF also has seasonal variability. Sprintall et al. (2009) have examined the ITF transport in three exit passages, namely Lombok and Ombai Straits, and Timor passage using INSTANT (International Nusantara Stratification AND Transport) data from January 2003 through December 2006. Their results show that seasonal variations of the ITF are influenced by the monsoon climate, with maximum ITF occurs during the SE monsoon. Furthermore, interannual variability also affects the ITF transport, which strengthened (weakened) during La Niña (El Niño) (Susanto et al., 2012; Susanto and



65 Song, 2015; Feng et al., 2018). In addition to El Niño–Southern Oscillation (ENSO) event, Pujiana, et al. (2019) have revealed that Indian Ocean Dipole (IOD) was also responsible for the anomalous ITF. They found a reduction in the ITF transport in 2016 due to an unprecedented negative IOD event. Feng et al. (2018) also reported the presence of decadal and interdecadal variations of the ITF transport, which is mostly due to the ITF responses to atmospheric forcing (trade winds) and oceanic adjustment in the Pacific (Meng et al., 2004; Feng et al., 2018).

70 In the offshore area of the SETIO, it has been reported that SEC in south of Java has intraseasonal variation with 60-day timescale (e.g., Quadfasel and Cresswell, 1992; Semtner and Chervin, 1992; and Bray et al., 1997). Further research carried out by Feng and Wijffels (2002) shows that baroclinic instability seems to be the main cause of intraseasonal variability in the SEC. Moreover, it is known that SEC in the southern Indian Ocean bifurcates at the east coast of Madagascar into the Northeast (NEMC) and Southeast Madagascar Currents (SEMC). Yamagami and Tozuka (2015) have investigated interannual variability  
75 of the SEC bifurcation along the Madagascar coast. Their results indicate that interannual variation of SEC bifurcation latitude and the NEMC and SEMC transports are correlated with Niño 3.4 index, with a lag of about 5–15 months. However, there is still no information concerning seasonal and interannual variations of SEC in the SETIO.

Regarding dynamics and characteristics of the SETIO, especially adjacent to the western coast of Sumatra and the southern coast of Java, all previous investigations are either based on numerical model, remote sensed data or velocity/moorings  
80 observations within the Indonesian seas or at the exit passages of Indonesian seas (Sunda, Lombok, Ombai, and Timor passages) which lead into the SETIO. There is almost no ocean current/velocity measurement within the SETIO. The observational velocity data are available only at limited points in space and time. The only velocity measurement in south of Java or in the SETIO region reported by Sprintall et al. (1999). The mooring was deployed south of Java in 200 m water depth from March 1997 to March 1998 at depths of 55 m, 115 m and 175 m velocity measurements, but only current meters at 115  
85 m and 175 m were fully working properly (Sprintall et al., 1999). Recently, there are some moorings to measure velocity and stratification deployed in the SETIO region. However, they have not been fully recovered nor published. Hence, due to limited of in situ velocity measurements in the SETIO, the detail dynamics and characteristics of SETIO regions have not been fully explained. These are the main motivations of the present study.

In addition, many studies of the current dynamic in the SETIO adjacent to the southern coasts of Sumatra and Java, which  
90 were carried out by the previous investigators mentioned above (i.e., Sprintall et al., 1999, 2010; Qu and Meyers, 2005; Iskandar et al., 2006), have been conducted on its intraseasonal and seasonal variabilities. It is necessary to acquire better and comprehensive insights of both spatial and temporal characteristics of the current circulation in the region. To the best of our knowledge, this important subject, especially in researches concerning features of zonal currents in the regions of SJC, ITF/SEC, and transition zone between the SJC and ITF/SEC as well as their interannual variation, has so far not been  
95 extensively studied in the region, both based on observations and numerical models. Hence, the aims of this paper are: (1) to further investigate basic features and mode structures of the current vertical profile time series and their temporal variability in the SETIO adjacent to the Sumatra-Java southern coasts using 64 years (1950–2013) data derived from simulated results of a 1/8° global version of the HYbrid Coordinate Ocean Model (HYCOM), (2) to better understand intraseasonal, seasonal,



and interannual variabilities of the current circulation in the area of study by using a combination of the Empirical Orthogonal  
100 Function (EOF) analysis and the Ensemble Empirical Mode Decomposition (EEMD) method (i.e., Huang et al, 1998; Wu and  
Huang, 2009; Shen et al., 2017, and references thereafter), and (3) to discuss exclusively the ocean current characteristics in  
the SETIO and subsequently elaborate their genesis.

## 2 Material and Methods

The HYCOM has been successfully used by previous investigators to simulate current circulation within the Indonesian waters  
105 (e.g., Gordon et al., 2008; Metzger et al., 2010; Shinoda et al., 2012). In this study, we analysed the HYCOM simulated currents  
with  $1/8^\circ$  horizontal resolution for the period of 64 years (1950-2013). Simulation results of the HYCOM version used in this  
study have been verified against several data and the verifications have been documented in our earlier publications (Hanifah  
and Ningsih, 2016). In addition to the aforementioned comparisons, in this paper we have performed comparisons between the  
moored RAMA (Research Moored Array for African-Asian-Australian Monsoon Analysis and Prediction) provided by the  
110 NOAA and HYCOM currents at two points (marked by points  $R_1$  and  $R_2$ ), and also comparisons between OSCAR (Ocean  
Surface Current Analysis Real-time) and the HYCOM currents at three points (marked by points  $O_1$ ,  $O_2$ , and  $O_3$ ), as shown in  
Fig. 1. The RAMA and OSCAR datasets have been provided by the NOAA ([https://www.pmel.noaa.gov/tao/data\\_deliv/deliv-  
nojava-rama.html](https://www.pmel.noaa.gov/tao/data_deliv/deliv-nojava-rama.html)) and Physical Oceanography Distributed Active Archive Center (PODAAC)  
([https://podaac.jpl.nasa.gov/dataset/OSCAR\\_L4\\_OC\\_third-deg](https://podaac.jpl.nasa.gov/dataset/OSCAR_L4_OC_third-deg)), respectively. The general agreement between the HYCOM  
115 currents and those of the moored RAMA is reasonably encouraging with correlation coefficient ( $r$ ) ranging from 0.40 to 0.57  
at point  $R_1$  (Figs. 1e-h) and 0.49 to 0.55 at point  $R_2$  (Figs. 1i-k), with the 95% significance level at both points approximately  
 $\pm 0.04$  and  $\pm 0.09$ , respectively. In addition, the comparisons between the HYCOM currents and the OSCAR data show general  
agreement as well at points  $O_1$  ( $r=0.65$ ),  $O_2$  ( $r=0.59$ ), and  $O_3$  ( $r=0.60$ ), with the 95% significance level at the three points  $\pm 0.13$   
(Figs. 1b-d). Further details of numerical model description of this applied HYCOM version can be found in Hanifah and  
120 Ningsih (2016).

In addition to the HYCOM simulated currents, to support analysis in this research, the Oceanic Niño and Dipole Mode Indices  
(ONI and DMI, respectively) were used to identify climate conditions and influences of interannual forcing associated with  
ENSO and IOD on interannual variability of the zonal currents in the study region. The ONI and DMI were obtained from the  
National Oceanic and Atmospheric Administration (NOAA) website (<http://www.cpc.ncep.noaa.gov/data/indices/>) and the  
125 Japan Agency for Marine Earth Science and Technology (JAMSTEC) website  
([http://www.jamstec.go.jp/frcgc/research/d1/iod/iod/  
dipole\\_mode\\_index.html](http://www.jamstec.go.jp/frcgc/research/d1/iod/iod/dipole_mode_index.html)), respectively. In addition, the wind fields  
derived from the NOAA (<https://www.esrl.noaa.gov/psd/data/gridded/data.ncep.reanalysis.derived.surface.html>) are also used  
to investigate the effects of local and remote winds on zonal current variations.

An Empirical Orthogonal Function (EOF) method (i.e., Kantha and Clayson, 2000; Hannachi, 2004) was then used to  
130 investigate the mode structure of the zonal current vertical profile and its temporal variability at points  $A_{SM}$ ,  $A_{WJ}$ , and  $A_{EJ}$



(Transect A), points  $B_{SM}$ ,  $B_{WJ}$ , and  $B_{EJ}$  (Transect B), and points  $C_{SM}$ ,  $C_{WJ}$ , and  $C_{EJ}$  (Transect C), as shown in Fig. 2. Moreover, temporal variability of the first EOF mode of zonal current was analysed by applying the EEMD method (i.e., Huang et al., 1998; Wu and Huang, 2009; Shen et al., 2017) for decomposing a signal into a series of intrinsic mode functions and investigating the zonal current variability in the SETIO region adjacent to the southern coasts of Sumatra-Java. Furthermore, a power spectral analysis (Emery and Thomson, 2001) was applied to the EEMD results to identify dominant periods of the zonal current variability in the study area.

### 3 Results

#### 3.1 Distinctive Features of Zonal Currents in the Study Area

As we are interested in investigating characteristics of main ocean currents those exist in the SETIO adjacent to the Sumatra-Java southern coasts, such as SJC, ITF, and SEC, in this study we only considered major component of those currents, namely the zonal current component in which it was analysed from surface to 800 m. The maximum depth of 800 m was chosen to capture the presence of prevailing ocean currents in the area of study and the surrounding regions, such as cores of the SJUC. For example, these cores in the Ombai Strait exist at about 400–800 m depth (Sprintall et al., 2010). Furthermore, based on monthly averaged surface currents over 64 years period (1950–2013), we analysed the zonal currents at three transects, namely Transects A, B, and C, which represent coastal region, transition zone between coastal and offshore regions, and the offshore one, respectively (Fig. 2). Transects A and C were selected with respect to the prevalence of ocean currents in the area of interest, representing near shore (SJC) and offshore (ITF/SEC) areas, respectively (Qu and Meyers, 2005; Fang et al., 2009; Ding et al., 2013). Moreover, in the present study, we have performed additional analyses of current characteristics on Transect B as the transition zone between the SJC region (Transect A) and ITF/SEC region (Transect C) due to the existence of distinctive features of zonal currents along the three transects (A, B, and C), as shown in Fig. 2.

To support our reasons for assigning the three transects, we have provided Fig. 3 (as an example), which clearly shows the distinctive features of near-surface zonal currents along the three transects. Dynamics of zonal surface currents on Transect A (Fig. 3c), especially along the southern coasts of Sumatra-Java ( $98^{\circ}$  E– $114^{\circ}$  E), show a complex interplay between remote wind forcings from both the equatorial Indian and Pacific Oceans and local wind. In general, there exist eastward-flowing currents during MAM and SON, which are probably attributed to Kelvin wave passage. Seasonal characteristic of zonal currents associated with local wind, which is eastward (westward) during DJF (JJA), especially along the southern coast of Java, can be clearly seen after 6–12 months band-pass filtering (figure not shown). In contrast, westward currents are dominant along Transect C (Fig. 3e). Meanwhile, although westward currents are quite dominant along Transect B, eastward currents are also present, especially at longitudes  $95^{\circ}$  E to  $107^{\circ}$  E (Fig. 3d).

Moreover, we also presented meridional sections of zonal current along the three longitudes (yellow lines in Fig. 2) to justify the selection of the locations for analysing zonal current characteristics, as shown in Fig. 4 (as an example). Figure 4 clearly shows the distinctive features of near-surface zonal currents along the three meridional sections, namely the coastal (SJC) area



(0° S – ~2.5° S at 98° E; ~7° S – 8.5° S at 107° E; and ~8° S – 9.5° S at 113° E), the transitional zone (~2.5° S – 9° S at 98° E; ~8.5° S – 10° S at 107° E; and ~9.5° S – 10.5° S at 113° E); and the offshore (ITF/SEC) area (~9° S – 12° S at 98° E; ~10° S – 12° S at 107° E; and ~10.5° S – 12° S at 113° E).

Furthermore, because we are specifically interested in zonal current characteristics off southern waters of Sumatra and Java, we selected three points on each transect, namely points  $A_{SM}$ ,  $A_{WJ}$ , and  $A_{EJ}$  on the Transect A; points  $B_{SM}$ ,  $B_{WJ}$ , and  $B_{EJ}$  on the Transect B; and points  $C_{SM}$ ,  $C_{WJ}$ , and  $C_{EJ}$  on the Transect C with respect to the distinctive features of zonal currents shown in Fig. 2, Figs. 3c-e, and Fig. 4. Here, the subscripts SM, WJ, and EJ of the nine selected points represent regions, which close to Sumatra, West Java, and East Java, respectively.

### 3.2 Climatological Current Fields

Figure 5 shows seasonal depth profiles of zonal current velocity and its average (the climatological current field) over the period of 64 years (1950–2013). Seasonal variations of the zonal currents were analysed during DJF, MAM, JJA, and SON at the nine observation points (Transects A to C), as shown in Fig. 2. It can be clearly seen in Fig. 5 that there are distinctive characteristics of the mean zonal currents on each transect (denoted by black lines in the Fig. 5). In the following subsections, we analysed the climatological current fields of each transect.

#### 3.2.1 Vertical Structure of Zonal Current along Transect A

On average, for the period 1950 through 2013, zonal climatological currents on the Transect A generally flow eastward from the sea surface to 100 m depth (Figs. 5a-f) and reach their maximum values of about  $0.03 \text{ m s}^{-1}$  ( $A_{SM}$ ),  $0.12 \text{ m s}^{-1}$  ( $A_{WJ}$ ), and  $0.16 \text{ m s}^{-1}$  ( $A_{EJ}$ ). It is suggested that the average zonal currents along this transect are mainly attributed to SJC and they show seasonal variations. During the SE monsoon (JJA), the strength of climatological eastward SJC off the southern coast of Java in the upper 20 m reduced (Figs. 5d-f). Meanwhile, during the NW monsoon (DJF), the currents along the Transect A (Figs. 5a-f) flow eastward in response to the prevailing northwesterly winds, namely in the upper 18 m ( $A_{SM}$ ), 45 m ( $A_{WJ}$ ), and particularly at point  $A_{EJ}$  the eastward current likely being present from the surface to 800 m (Fig. 5c).

Moreover, Fig 5d-f show that during the NW monsoon the eastward currents at  $A_{EJ}$  are stronger than those at  $A_{SM}$  and  $A_{WJ}$ . The stronger current at  $A_{EJ}$  may exist as a consequence of the stronger mean NW monsoon at  $A_{EJ}$  compared with those at  $A_{SM}$  and  $A_{WJ}$  (Fig. 7). In general, the mean eastward currents along Transect A during DJF were attributed to winds. Wind-driven currents appear to be a reasonable cause for the eastward currents at  $A_{SM}$  and  $A_{WJ}$ , at which the currents are evident at depths < 100 m. Interestingly, however, at  $A_{EJ}$ , the eastward current occurs up to ~800 m. Other physical processes may account for the eastward currents at  $A_{EJ}$ , particularly those at depth beneath 100 m. The SJC and SJUC are defined as the surface current in the upper 150 m and the subsurface current beneath 150 m down to 1000 m, respectively (Iskandar et al., 2006) and they are attributed to the arrival of a downwelling Kelvin wave at the south coast of Java (e.g., Sprintall et al., 1999, 2000; Iskandar



195 et al., 2006). Downwelling Kelvin waves originating in the equatorial Indian Ocean during the transitional monsoons propagate along the coasts of western Sumatra and southern Java with phase speeds ranging from 1.5 to 2.9 m s<sup>-1</sup> (e.g., Sprintall et al., 2000; Syamsudin et al., 2004; Iskandar et al., 2005). These phase speeds indicate that the downwelling Kelvin waves will arrive at A<sub>EJ</sub> in 21 – 41 days. In this case, downwelling Kelvin waves generated during the monsoon transition period in November may arrive at A<sub>EJ</sub> in December/January. Therefore, in addition to the local eastward winds, the downwelling Kelvin waves may also contribute to the eastward currents at A<sub>EJ</sub> during the NW monsoon, including those at depth beneath 100 m. At a depth of 100 m, there is a maximum westward current at A<sub>WJ</sub> during DJF with velocity of about 0.1 m s<sup>-1</sup> (Figs. 5b and 5e). Here, we suggest that ITF is the cause of the westward current at 100 m at A<sub>WJ</sub> during the DJF. In regard to the ITF, Fig. 3 of Sprintall et al. (2010) shows cores of subsurface maximum ITF extending from 100 m to 250 m depth in the northern part of the Ombai Strait and from 100 m to 800 m depth at the southern part of the strait during DJF. Meanwhile, the influence of ITF on the zonal current at A<sub>EJ</sub> at 100 m is weaker as a consequence of the stronger NW monsoon at A<sub>EJ</sub> compared with those at A<sub>WJ</sub>, so that the current flows rather eastward at A<sub>EJ</sub> during DJF (Figs. 5b-c, 5e-f, and Fig. 7).

To further investigate which one is more influential between the ITF and the NW monsoon to force the zonal current at the A<sub>WJ</sub> and A<sub>EJ</sub> at 100 m depth, we have carried out correlation between the zonal current at both points (each at depth of ~100 m) and each the NW zonal wind and the zonal current representing subsurface (~200 m) maximum ITF in the southern Ombai Strait (Table 1). Here, the ITF in the southern part of the Ombai Strait was chosen for carrying out the correlation because the ITF flows mainly through the southern part of the passage (Sprintall et al., 2010). It is found that the subsurface maximum ITF during DJF exists at a depth of about 200 m in both the northern and southern parts of the Ombai Strait and it is stronger during DJF than JJA in both parts of the strait (Fig. 3 of Sprintall et al., 2010). In this study, the DJF zonal currents in the period of 2004 through 2006 in the southern Ombai Strait derived from the INSTANT program (<http://www.marine.csiro.au/~cow074/instantdata.htm>) were used for the correlation analysis.

It is found that during DJF the zonal current at A<sub>WJ</sub> at 100 m shows high correlation with the subsurface (~200 m) maximum ITF in the southern Ombai Strait, whereas its correlation with the NW zonal wind is weak (Table 1). Moreover, although during DJF the correlations between the zonal current at A<sub>EJ</sub> at 100 m and each NW zonal wind and subsurface (~200 m) maximum ITF in the southern Ombai Strait are below the significance level, the NW zonal wind is more influential to force variation of zonal current at A<sub>EJ</sub> at 100 m than the ITF. Hence, during DJF we suggest that the westward current simulated at A<sub>WJ</sub> at 100 m is ITF-related, whereas that at A<sub>EJ</sub> is relatively NW zonal wind-related. As already discussed, in addition to the local eastward winds during DJF, it is suggested that the arrival of downwelling Kelvin waves in December/January at A<sub>EJ</sub> may contribute to a net eastward current across the water column, which in turn reducing the influence of ITF at this point. Our simulation shows that during the monsoon transitions (MAM and SON), SJC is eastward and intensified by the propagation of coastal Kelvin waves associated with the Wyrki Jet (WJ) in the equatorial Indian Ocean, which is forced by the local equatorial zonal winds during both monsoons. These waves propagate along the Sumatra-Java coast (i.e., Sprintall et al., 2000; Druskha et al. 2010, Iskandar et al. 2009) and some portions propagate northward into the Lombok and Makassar Straits (Susanto et al., 2000; 2012; Pujiana et al., 2013), whereas the remaining parts continue eastward (Syamsuddin et al.,



2004). Furthermore, the present study shows that the eastward current during SON is stronger than that during MAM, which  
230 is consistent with mooring observation in the Makassar Strait (Susanto et al., 2012; their Fig. 3). The stronger eastward current  
during SON was supposed to be attributed to the faster and more intense climatological WJ during SON than that during MAM  
(Knox, 1976; McPhaden, 1982; Han et al., 1999; Qiu et al., 2009; McPhaden et al., 2015; Figs. 1d and 2e of Duan et al., 2016)  
and also associated with the stronger wind forcing over the eastern equatorial Indian Ocean during the SON compared with  
the MAM period (figure not shown), which is responsible for the WJ. The eastward current during SON reaches its maximum  
235 velocity of about  $0.05 \text{ m s}^{-1}$  ( $A_{SM}$ ),  $0.23 \text{ m s}^{-1}$  ( $A_{WJ}$ ), and  $0.20 \text{ m s}^{-1}$  ( $A_{EJ}$ ) at  $\sim 30\text{--}50 \text{ m}$  depths (cyan lines in Figs. 5d-f).  
Furthermore, results of this study show that a maximum value of the eastward current forced by a Kelvin wave is found at a  
certain depth (at  $\sim 30\text{--}50 \text{ m}$  depths; Figs. 5a-f) and it is supposed to be attributed to a baroclinic Kelvin wave. The baroclinic  
Kelvin wave propagating vertically and horizontally along its waveguide can exert energy the most at a certain depth (Drushka  
et al., 2010; Pujiana et al., 2013). According to laboratory experiment observation conducted by Codiga et al. (1999) and  
240 Hallock et al. (2009), Kelvin wave can be trapped in a slope and propagates along an isobath. This phenomenon is known as  
slope-trapped baroclinic Kelvin wave. Moreover, Kelvin wave which propagates along continental slope with strong  
stratification can cause strong current velocity. Codiga et al. (1999) also found that this slope Kelvin wave is formed after  
encountering a canyon-like bathymetry. Meanwhile, Pujiana et al. (2013) shows that Kelvin wave propagation from Lombok  
Strait to Makassar Strait, across Sunda continental slope, is along isobaths at depths greater than 50 m. In this present study,  
245 eastward current along the Transect A has maximum current velocity at depth  $\sim 30\text{--}50 \text{ m}$ . Therefore, it is suggested that this  
maximum eastward current at  $\sim 30\text{--}50 \text{ m}$  depth associated with slope-trapped Kelvin wave, which propagates at that depth  
along the southern coasts of Sumatra and Java.

### 3.2.2 Vertical Structure of Zonal Current along Transect B

250 In the transition region (Transect B), average zonal current (the climatological current field) shows different characteristics at  
each point (denoted by black lines in Figs. 5g-l). The average current at  $B_{SM}$  is eastward, while at points  $B_{WJ}$  and  $B_{EJ}$  it is  
westward. During NW and transitional periods of the monsoon, zonal current at  $B_{SM}$  flows eastward and reaches its maximum  
velocity of about  $0.12 \text{ m s}^{-1}$  at a depth of 40 m within the period of SON (Fig. 5j). Meanwhile, during SE monsoon, the zonal  
current at this point flows westward. In contrast to the mean zonal currents along Transect A, it seems that the average zonal  
255 current field at  $B_{SM}$  is not attributed to SJC. The reason is the  $B_{SM}$  location, which is far from the coasts of Mentawai Islands and  
Enggano Island off the western coast of Sumatra by 430 km. This distance is more than Rossby radius of deformation at this  
latitude ( $\sim 90 \text{ km}$ ). Thereby, Kelvin waves, which affect the SJC variations, do not exist at this point. We suggest that the  
current variability at  $B_{SM}$  is influenced by tropical current systems in the Indian Ocean, such as the Equatorial Counter Current  
(ECC), Southwest Monsoon Current (SWMC), and WJ. Here, we displayed seasonal averaged surface currents over 64 years  
260 (1950–2013) and schematics of the tropical current systems in the Indian Ocean as supporting evidence (Fig. 6).





Figure 6 shows that  $B_{SM}$  is located at an area, which is affected by the ECC, SWMC, and WJ. It can be seen in the Fig. 6a that during DJF, surface currents along the equatorial Indian Ocean is dominated by the westward North Equatorial Current (NEC) and the eastward ECC. Meanwhile, during JJA (Fig. 6c), the NEC disappears and the ECC becomes absorbed into the SWMC, which dominantly flows eastward in the northern Indian Ocean (Tomczak and Godfrey, 1994). In addition, during the transitional periods (MAM and SON), the WJ is generated and it causes a strengthening of eastward flows along the equatorial Indian Ocean (Figs. 6b and 6d). This explains the cause of climatological current at  $B_{SM}$  flows eastward and reaches its maximum velocity during SON and MAM. These currents (the ECC, SWMC, and WJ) flow eastward before they turn and some part of their flow feed into the SEC in the southern Indian Ocean.

Furthermore, it is suggested that the mean westward currents at the points  $B_{WJ}$  and  $B_{EJ}$  are more dominated by the ITF (shown by black lines in Figs. 5h-i and 5k-l). Based on observation in the exit passages (Lombok Strait, Timor Passage, and total ITF along exit passages), ITF in JJA is stronger than that in DJF (e.g., Sprintall et al., 2009). In this study, however, it is found that westward currents at the points  $B_{WJ}$  and  $B_{EJ}$  are stronger during DJF than JJA. This anomaly of the ITF seasonality at both points is also found in the Ombai Strait as documented by Sprintall et al. (2009, their Table 3; 2010, their Fig. 3). Moreover, Sprintall et al. (2010) found cores of subsurface maximum ITF during DJF extending from 100–250 m (100–800 m) depth at the northern (southern) part of the strait. In this study, this seasonal feature of the subsurface maximum ITF is also found at both  $B_{WJ}$  and  $B_{EJ}$  in which the corresponding westward currents at these points reach their maximum values at ~100 m depth and the maximum westward currents are stronger during DJF than JJA (Figs. 5h-i and 5k-l). Hence, we suggest that the primary driver for zonal westward current at  $B_{WJ}$  and  $B_{EJ}$  is the ITF coming from the Ombai Strait. To confirm the above relation, we have calculated the correlation between zonal westward currents at a depth of ~100 m each at points  $B_{WJ}$  and  $B_{EJ}$  and those representing subsurface (~200 m) maximum ITF in the southern Ombai Strait (Sprintall et al., 2010). The correlation coefficient between the zonal westward currents at ~100 m at the  $B_{WJ}$  and those of the southern Ombai Strait is 0.77, while it is 0.58 for the  $B_{EJ}$  with the 95% significance level approximately  $\pm 0.33$ . This study shows that the zonal westward currents at 100 m depth at both  $B_{WJ}$  and  $B_{EJ}$  have a strong correlation with the subsurface (~200 m) maximum ITF in the southern Ombai Strait, confirming that the ITF flowing from the Ombai Strait is the primary driver for zonal westward current at both  $B_{WJ}$  and  $B_{EJ}$ . Nevertheless, the cause of the anomalous behaviours of seasonality of the ITF in the Ombai Strait and of the corresponding westward currents at  $B_{WJ}$  and  $B_{EJ}$ , in which the ITF and currents are stronger during DJF than JJA, is still unclear. Therefore, further study is required to increase our understanding of this challenging matter.

### 3.2.3 Vertical Structure of Zonal Current along Transect C

Current characteristics in the offshore region of the study area (Transect C) generally show similarities at all points ( $C_{SM}$ ,  $C_{WJ}$ , and  $C_{EJ}$ ), as shown in Figs. 5m-r. The current at these points flows westward throughout the year and has average velocity around 0.20–0.35  $m s^{-1}$  in the upper 100 m. Under such characteristics we supposed that the westward current on the Transect C is the SEC, which encounters with the ITF flowing out from the Lombok and Ombai Straits, and Timor Passage. The



295 HYCOM westward currents along the Transect C (Figs. 5m-r) are stronger during JJA than DJF, which are associated with seasonal characteristics of the ITF in Lombok Strait, Timor Passage, and of the total ITF through the Lombok and Ombai Straits, and Timor Passage (Potemra, 1999; Sprintall et al., 2009). The westward current on the Transect C (Figs. 5p-r) reaches its maximum value of about  $0.42 \text{ m s}^{-1}$  ( $C_{SM}$ ),  $0.48 \text{ m s}^{-1}$  ( $C_{WJ}$ ), and  $0.31 \text{ m s}^{-1}$  ( $C_{EJ}$ ).

### 3.3 Zonal Current Variability

300 EOF analysis gives vertical mode structures (spatial mode) and their normalized temporal mode variabilities relative to the mean which influence zonal current variability in the study area. Before performing the EOF analysis, the average value of the current data has been removed (solid black lines in the Figs. 5a-r). Table 2 displays dominant variances at the nine observation points. From the Table 2, the first three modes at each point already represent  $\geq 95\%$  of the total variance. In fact, the first two modes at each point (except at points  $A_{SM}$  and  $A_{EJ}$ ) already represent  $\geq 91\%$  of the total variance. In this paper, we only  
305 consider the first modes of EOF analysis since their percent variances (except at point  $A_{SM}$ ) are more than 50% of the total variance. Temporal variability of the first EOF mode (EOF1) was then analysed by using the EEMD method to decompose the signal. In this study, the EOF and EEMD analyses of currents are only conducted at one point on each transect, namely  $A_{WJ}$  (Transect A),  $B_{SM}$  (Transect B), and  $C_{EJ}$  (Transect C). The  $A_{WJ}$ ,  $B_{SM}$ ,  $C_{EJ}$  points were chosen to investigate SJC variability, interannual variability in the open SETIO, and SEC and ITF variabilities, respectively.

310 The EEMD analysis of the first temporal EOF mode provides 10 modes/signals in which the first signal of the EEMD result is the summation of the second to tenth signals, which is the same as the EOF first temporal mode of zonal currents. Meanwhile, the second–sixth signals of the EEMD result vary from intraseasonal to interannual variabilities. The remaining signals of EEMD result show the long-term trend.

#### 315 3.3.1 Intraseasonal, Semiannual, and Annual Variations

Figures 8a–b show vertical structure and temporal variability of the EOF1 (58% of total variance) at  $A_{WJ}$ , respectively. In order to see more clearly temporal variation of the EOF1 in Fig. 8b, we have provided the last eight-year period of the EOF first temporal mode (Fig. 8c, as an example). Current velocity variability relative to the mean flow can be obtained by multiplying the vertical mode structure (Fig. 8a) with the temporal variability (Fig. 8b).

320 Intraseasonal, semiannual, and annual variabilities of the EOF first temporal mode at  $A_{WJ}$  as results of the EEMD analysis are displayed in Figs. 8d-f, where their power spectra (left) show maximum energy at 3-month, 6-month, and 12-month periods, respectively. At this point, the highest power spectrum occurs at semiannual variability (Fig. 8e). In this figure (right), the semiannual variability of the EOF first temporal mode at  $A_{WJ}$  clearly shows the presence of an eastward anomaly of the zonal current during the MAM and SON, which may be forced by Kelvin waves associated with the WJ in the equatorial Indian  
325 Ocean (Wyrтки, 1973; Quadfasel and Cresswell, 1992; Sprintall et al., 2000, 2010). Meanwhile, the anomaly of the zonal



current at  $A_{WJ}$  is westward during JJA in response to the prevailing southeasterly local winds during the SE monsoon. On the other hand, during DJF, the anomaly of the zonal current at  $A_{WJ}$  is not associated with the prevailing northwesterly local winds during the NW monsoon, where the current anomaly is westward during this monsoon (Fig. 8e). As already discussed in Sect. 3.2 (Table 1 and Fig. 7), this may be attributed to the ITF that has more influence on variation of zonal current at  $A_{WJ}$  during  
330 DJF than the NW local wind.

Similar to  $A_{WJ}$ , the first mode of EOF vertical structure and its temporal variability (64% of total variance) at  $B_{SM}$  show seasonal pattern (Figs. 9a-c). It is also found that signal with 6-month (semiannual) period is quite dominant at  $B_{SM}$  (Fig. 9e). In order to see more clearly the seasonal variation, we have provided a probability distribution function of the EOF1 of zonal currents for each of the NW, SE, and transition seasons at  $B_{SM}$  at a depth of ~40 m (Fig. 12). The 40 m depth was selected as  
335 an example because the most obvious seasonal variation of currents presents at this depth. It is found that variation of zonal current at  $B_{SM}$  is dominantly eastward during DJF (Fig. 12a) and this eastward current is enhanced during MAM and SON (Figs. 12b and d), which may be attributed to the tropical current systems in the Indian Ocean (ECC, SWMC, and WJ). Meanwhile, during JJA (Fig. 12c), the dominance of eastward current reduces, and the current tends to be dominantly westward.

340 Figures 10a-c show the first mode of EOF vertical structure and its temporal variability (72% of total variance) at  $C_{EJ}$ . In general, anomaly of the zonal current at  $C_{EJ}$  is westward, which is supposed to be associated with the meeting of SEC driven by trade winds and the ITF at this region. The EEMD analysis of the EOF1 of zonal current at  $C_{EJ}$  also shows intraseasonal-interannual variabilities (Figs. 10d-g), where it is found that interannual timescale dominates the zonal current variation at  $C_{EJ}$  (0.017 power/year).

345 To obtain a better understanding of the zonal current characteristics at  $A_{WJ}$ ,  $B_{SM}$ , and  $C_{EJ}$ , we have summarized maximum energy density of zonal currents at intraseasonal, semiannual, annual, and interannual timescales that exists at each point based on power spectrum calculation in Figs. 8-10 (Table 3). It is shown that the zonal currents at  $A_{WJ}$  are consecutively dominated by semiannual, intraseasonal, and annual signals, while interannual signal is weaker than them at this point. Furthermore, although semiannual and intraseasonal signals are dominant at  $B_{SM}$ , there is pronounced interannual variation of the zonal  
350 current at this point. In contrast, the zonal current variability at  $C_{EJ}$  is dominated by interannual signal.

Furthermore, based on the power spectrum calculation shown in Fig.10 (Table 3), it is found that intraseasonal variability of the SEC (zonal current at  $C_{EJ}$ ) is also prominent (about 0.012 power/year) in addition to the interannual signal (about 0.017 power/year). Meanwhile, based on sea level anomaly data in the period of October 1992 to the end of 1998 (about 6 years), Feng and Wijffels (2002) suggested that the strongest intraseasonal variability in the SETIO occurs in the SEC during the July-  
355 September season and baroclinic instability seems to be the leading cause. On the other hand, in this study, we found that the strongest intraseasonal variability occurs in the SJC (zonal current at  $A_{WJ}$ ). This different result seems due to differences in the length of data used in this study (64 years) and that in Feng and Wijffels (2002) (6 years). In addition, in this study, we analyzed intraseasonal variability from the signal of the EOF first temporal mode of zonal currents (accounting for 58%, 64%, and 72% of total variance at  $A_{WJ}$ ,  $B_{SM}$ , and  $C_{EJ}$ , respectively), whereas Feng and Wijffels (2002) analyzed the intraseasonal variation



360 from standard deviation of the 6-year sea level anomaly data based on the 100-day high-pass filtered altimeter data during the four seasons (January-March, April-June, July-September, and October-December). Moreover, some of the difference may also be due to the fact that altimeter data do not resolve coastal processes well. However, further study is required to address this issue.

### 365 3.3.2 Interannual Variations

In this study, it is found that the most energetic zonal current variations of EOF1 at  $A_{WJ}$ ,  $B_{SM}$ , and  $C_{EJ}$  exist at ~30 m depth (Figs. 8a, 9a, and 10a). To investigate exclusively the ocean currents at interannual timescale, lagged correlation analyses have been applied between the zonal currents at a depth of about 30 m at points  $A_{WJ}$ ,  $B_{SM}$ , and  $C_{EJ}$  and each of the climatic indices (e.g., ONI and DMI), as shown in Table 4. The ONI and DMI indices from 1950 to 2013 used in this study are shown in Fig. 370 11.

The analysis of lagged correlation shows that the currents at  $B_{SM}$  and  $C_{EJ}$  show positive correlations with the ONI, namely  $r(18)=0.24$  and  $r(4)=0.27$ , respectively, with the 95% significance level approximately  $\pm 0.07$ , indicating that an El Niño (La Niña) event is favourable for an eastward (westward) currents at these points (Figs. 9g and 10g) and also pointing out that ITF transport is lower (higher) during El Niño (La Niña) events (Fieux et al., 1996; Meyers, 1996; Gordon and Susanto, 1999; 375 Ffield et al., 2000; Susanto et al., 2001; Susanto and Gordon, 2005; Susanto et al., 2012; Liu et al., 2015; Susanto and Song, 2015; and Zhang et al., 2016). ENSO events seem to have a strongest influence on the zonal current variability at  $C_{EJ}$  (Table 4), which is located close to the exits of the ITF. The ENSO signals penetrate into the SETIO mainly through the equatorial Pacific and coastal ocean Indonesian waveguides (Wijffels and Meyers, 2004; Zhang et al., 2016). Meanwhile, the present study shows that the correlation between the zonal current at  $A_{WJ}$  and ONI is weak and below the significance level.

380 Furthermore, negative correlation is found between IOD and zonal currents at  $A_{WJ}$  [DMI- $U$ :  $r(9)=-0.09$ ],  $B_{SM}$  [DMI- $U$ :  $r(1)=-0.28$ ], and  $C_{EJ}$  [DMI- $U$ :  $r(11)=-0.13$ ]. The correlation analysis indicates that IOD is most influential to force interannual variation of the zonal currents at  $B_{SM}$ , with the IOD leading the zonal currents by 1 month. The influence of interannual phenomenon at  $B_{SM}$ , such as IOD, is stronger and relatively instantaneous than that at points  $C_{EJ}$  and  $A_{WJ}$ . This may due to the location of  $B_{SM}$ , which is close to the center of eastern pole of the IOD (100° E, 5° S; Saji et al., 1999). In contrast to ONI, 385 there is IOD signals at  $A_{WJ}$  although the IOD signals at this point are weak compared to  $B_{SM}$ , and  $C_{EJ}$  (Table 4). This indicates that some of the IOD signals are coastally trapped.

Table 5 lists extreme and neutral years and their concurrent events through 1950-2013. To further investigate interannual variation of zonal current, we summarized presence of major climate modes (ENSO and/or IOD) and the corresponding current anomalies at the points of  $B_{SM}$  and  $C_{EJ}$  (Table 6) based on the lagged correlation analyses in Table 4 and the interannual 390 variations of zonal current (Figs. 9g and 10g), and the ONI and DMI (Fig. 11), respectively. In the Table 4, the ONI- $U$  and DMI- $U$  correlations are independent of IOD and of ENSO, respectively. Meanwhile, the current anomalies, which are attributed to the presence of major climate modes (ENSO and/or IOD) shown in the Table 6, could be forced by the influences



of ENSO or IOD, or the combined effect of them. In this study, the amounts of respective contribution values of ENSO and IOD, or the combined effect of them on the current anomalies shown in the Table 6 are still unknown. Further studies are thus required to more quantitatively determine the contribution values of each of climate modes on zonal current variations in the study area as well as their possible teleconnection. The last mode (Figs. 8h, 9h, and 10h) represents long-term trend which may be associated with long-term internal variability within the Indian Ocean or remote forcing from the Pacific Ocean and it may discuss in detail in future paper.

### 3.3.3 Relationship of the Zonal Current Variations at $A_{WJ}$ , $B_{SM}$ , and $C_{EJ}$ to Both Remote and Local Wind Forcings

To confirm possible influences of wind forcings on dominant variations of zonal current at  $A_{WJ}$ ,  $B_{SM}$ , and  $C_{EJ}$ , we have calculated the correlation between them. In this study, it is found that the zonal currents at  $A_{WJ}$  (close to the shore) are dominated by semiannual signal (0.140 power/year; Table 3). The semiannual variations of the zonal current at  $A_{WJ}$  show the presence of an eastward anomaly of the zonal current during MAM and SON, which may be associated with Kelvin waves forced by winds over the equatorial Indian Ocean (Wyrтки, 1973; Quadfasel and Cresswell, 1992; Sprintall et al., 1999, 2000, 2010). Furthermore, we have calculated the correlation between zonal currents in the upper layer (30 m) at  $A_{WJ}$  and zonal winds for the semiannual signals extracted using the EEMD method (Fig. 13). The 30 m upper layer flows at  $A_{WJ}$  show a strong positive correlation with the zonal winds over the equatorial Indian Ocean, with the winds leading the current by approximately one month. The positive correlation indicates that the flows are to the east when the winds blow from the west to the east, and vice-versa for the easterly wind. The one-month lag of the flows at  $A_{WJ}$  with the zonal winds in the equatorial Indian Ocean is in agreement with the expected arrival time of Kelvin waves at this point, suggesting that it is of about 18 – 35 days with phase speeds ranging from 1.5 to 2.9  $m s^{-1}$  (e.g., Sprintall et al., 2000; Syamsudin et al., 2004; Iskandar et al., 2005). Interestingly, there is also a weaker positive correlation of the 30 m upper layer flows at  $A_{WJ}$  at lag of about one month with zonal trade winds in the western equatorial Pacific Ocean (WEPO) at semiannual timescale, indicating that a strengthening (weakening) of easterly trade winds over the WEPO is favourable for anomalous westward (eastward) currents at  $A_{WJ}$ . The strengthening of easterly trade winds over the WEPO will increase sea level in the northern waters of West Papua and New Guinea, enhancing eastward pressure gradient across the Indonesian seas and forcing strengthened ITF transport. Since the currents at  $A_{WJ}$  are strongly correlated to the ITF (Table 1), it is suggested that this possible dynamic could result in anomalous westward currents at  $A_{WJ}$ , and vice-versa for the weakening winds over the WEPO.

Semiannual (0.135 power/year) signal of current variations is also dominant at  $B_{SM}$  but it is weaker than that at  $A_{WJ}$ . In addition, there is pronounced interannual (0.012 power/year) variation of the zonal current at  $B_{SM}$  (Table 3 and Fig. 9g), in which IOD is most influential to force interannual variation of currents at this point (at 30 m), (Table 4). Like at  $A_{WJ}$ , we also look for the relationships of the upper layer flow (30 m) at  $B_{SM}$  with the zonal winds but for the interannual signal obtained using the EEMD method (Fig. 14). At interannual timescale, the 30 m upper layer flows at  $B_{SM}$  show a strong positive correlation with the zonal winds over the eastern tropical Indian Ocean, in which the response of the flows to the zonal winds are relatively



instantaneously at a lag of about one month (Fig. 14). Location of the zonal winds affecting interannual variations of the upper layer flows at  $B_{SM}$  is in accord with the eastern pole region of IOD ( $90^{\circ}E-110^{\circ}E$ ,  $10^{\circ}S-0^{\circ}S$ ; Saji et al. 1999). Furthermore, as already explained, the zonal current variability at  $C_{EJ}$  (close to the exits of the ITF) is dominated by interannual (0.017 power/year) signal in which the influence of ENSO is strongest at this point at depth of 30 m (Table 4). To enhance our understanding of possible relationship of zonal currents at  $C_{EJ}$  to wind forcings at interannual timescale, we have also calculated the correlation between the upper layer flow (30 m) at  $C_{EJ}$  and the zonal winds, particularly in the Pacific Ocean. Like at  $B_{SM}$ , the interannual signals of both flow and winds are extracted using the EEMD method. At interannual timescale, the flows at  $C_{EJ}$  at 30 m show a significant positive correlation with the local winds and the remote winds over the equatorial Pacific Ocean, in which the response of the flows to the zonal winds are about 4 to 6 months. In addition, we also found that the 4-month lag signals are stronger than the signals with the 5 to 6 months of lag. Figure 15 shows a correlation map between the Pacific winds and the currents at  $C_{EJ}$  in the case of a 4-month lag.

#### 4 Conclusions

Basic features of zonal currents and their temporal variability in the SETIO region adjacent to the Sumatra-Java southern coasts have been studied using global HYCOM output over the course of 1950 – 2013. There exist distinctive features of zonal currents in coastal (the SJC) region, offshore (the ITF/SEC) region, and transition zone between coastal and offshore regions of the SETIO. In general, surface zonal currents on Transect A (the SJC region), especially along the southern coasts of Sumatra-Java ( $98^{\circ}E-114^{\circ}E$ ), show seasonal characteristics, which are eastward (westward) during DJF (JJA). Moreover, the eastward-flowing currents are enhanced during MAM and SON associated with the propagation of coastal Kelvin waves. On the other hand, westward currents are dominant along Transect C (the ITF/SEC region). Meanwhile, although westward currents are quite dominant along Transect B (the transition zone between the SJC region and ITF/SEC region), eastward currents are also present, especially on longitudes  $95^{\circ}E$  to  $107^{\circ}E$ .

In the period of 1950 through 2013, the mean (climatological) current velocity of SJC on Transect A is dominantly eastward. We found that both remote and local wind forcings as well as seasonal conditions are necessary to explain the current variability in the study area. During JJA, the strength of climatological eastward SJC reduced and the SJC in the upper 100 m along the southern coast of Java, at a certain period of time, flowed westward in response to the prevailing southeasterly local winds during those months. At the depth 100 m, there is a maximum westward current at  $A_{WJ}$  during DJF with velocity of about  $0.1 \text{ m s}^{-1}$ , in which the current at the  $A_{WJ}$  shows high correlation with the subsurface (200 m) maximum ITF in the southern Ombai Strait (remote forcing), whereas its correlation with the NW local wind is weak. Otherwise, it is found that the NW zonal wind is more influential to force variation of zonal current at  $A_{EJ}$  than the ITF. Therefore, it is suggested that the westward current simulated at  $A_{WJ}$  at 100 m during DJF is ITF-related, whereas that at  $A_{EJ}$  at 100 m is relatively NW zonal wind-related.

Moreover, it is found that the average (climatological) current at  $B_{SM}$  is eastward, while at points  $B_{WJ}$  and  $B_{EJ}$  it is westward, suggesting that the mean eastward current at  $B_{SM}$  is influenced by tropical current systems in the Indian Ocean, such as the



ECC, SWMC, and WJ, whereas the mean westward currents at the points  $B_{WJ}$  and  $B_{EJ}$  are more dominated by the ITF. In contrast, current characteristics on Transect C (offshore region) generally show similarities at all points ( $C_{SM}$ ,  $C_{WJ}$ , and  $C_{EJ}$ ), where the current along this transect flows westward throughout the year, confirming that Transect C is the SEC/ITF region. Seasonality of the westward current on the Transect C agrees well with that of ITF in Lombok Strait, Timor Passage, and through the three exit passages (the total ITF through the Lombok and Ombai Straits, and Timor Passage) that it is stronger during JJA than DJF.

In this study, the predominant variation content of the zonal current anomalies in the region is quantitatively identified, varying from intraseasonal to interannual timescales. The analysis indicates that the zonal currents at  $A_{WJ}$  (close to the shore) are consecutively dominated by semiannual (0.140 power/year), intraseasonal (0.070 power/year), and annual (0.038 power/year) signals, in which interannual (0.003 power/year) signal is weaker than them at this point. Moreover, although semiannual (0.135 power/year) and intraseasonal (0.033 power/year) signals are dominant at  $B_{SM}$  (close to the center of eastern pole of the IOD), there is pronounced interannual (0.012 power/year) variation of the zonal current at this point. In contrast, the zonal current variability at  $C_{EJ}$  (close to the exits of the ITF) is dominated by interannual (0.017 power/year) signal. Nevertheless, in addition to the interannual signal, the power spectrum analysis shows that intraseasonal variability of the zonal current (SEC) at  $C_{EJ}$  is also prominent (0.012 power/year). This may be attributed to the baroclinic instability, which seems to be the main cause of the prominent intraseasonal variation at  $C_{EJ}$  (Feng and Wijffels, 2002).

The lagged correlation analysis shows that there are positive correlations between ENSO and current anomalies at  $B_{SM}$  [ $r(18)=0.24$ ] and at  $C_{EJ}$  [ $r(4)=0.27$ ], indicating that an El Niño (La Niña) event is favourable for an eastward (westward) current at these points. In response to IOD events, the analysis shows that IOD has negative correlations with current anomalies at  $B_{SM}$  [ $r(1)=-0.28$ ] and at  $C_{EJ}$  [ $r(11)=-0.13$ ], pointing out that there exists an eastward (westward) anomaly of the currents during negative (positive) DMI, which is associated with northwesterly (southeasterly) wind over the study area. Moreover, it is found that IOD is most influential to force interannual variation of the zonal current at  $B_{SM}$  since it is located close to the center of eastern pole of the IOD, while ENSO events seem to have a strongest influence on the zonal current variability at  $C_{EJ}$ , probably due to its location near the exits of the ITF.

This study has quantified changes in variability of zonal current anomalies in the SETIO on timescales ranging from intraseasonal to interannual. Nevertheless, it is necessary to perform future work, which includes detailing the forcing mechanisms as well as investigating decadal variability and determining the cause of the long-term signals to gain a better understanding of these interesting topics.

### Data Availability

The data used in this study are deposited at <https://www.oceanography.fitb.itb.ac.id/member/nsn/>



### Author Contribution

490 Primary author NSN formulated research goals and aims, developed methodology, conducted investigation process, designed model, and prepared the published work. SLS maintained research data, prepared data presentation, and drafted the initial manuscript. RDS supervised the research project and EEMD methodology. FH designed model simulation and validated the model results.

### Competing Interest

495 The authors declare that they have no conflict of interest.

### Acknowledgements

The authors would like to gratefully acknowledge data support from the following institutions. The moored RAMA current is provided by the NOAA ([https://www.pmel.noaa.gov/tao/data\\_deliv/deliv-nojava-rama.html](https://www.pmel.noaa.gov/tao/data_deliv/deliv-nojava-rama.html)), while the INSTANT current is available at the INSTANT Web site (<http://www.marine.csiro.au/~cow074/instantdata.htm>). The wind fields are obtained from the NOAA (<https://www.esrl.noaa.gov/psd/data/gridded/data.ncep.reanalysis.derived.surface.html>). The ONI is provided by the NOAA/CPC at <http://www.cpc.ncep.noaa.gov/data/indices/>. The DMI is from the JAMSTEC at [http://www.jamstec.go.jp/frgcr/research/d1/iod/iod/dipole\\_mode\\_index.html](http://www.jamstec.go.jp/frgcr/research/d1/iod/iod/dipole_mode_index.html). Meanwhile, the HYCOM simulation results are available at Research Group of Oceanography-ITB, Faculty of Earth Sciences and Technology, Bandung Institute of Technology (<https://www.oceanography.fitb.itb.ac.id/member/nsn/>). We would like to thank the support given by the  
505 DIKTI under Basic Research Grant 2019 and Program of World Class Professor (WCP) 2018, for funding this works and making the writing of this paper possible. R. Dwi Susanto is supported WCP-2018 and National Aeronautics and Space Administration (NASA) grant #80NSSC18K0777 and Jet Propulsion Laboratory-NASA subcontract #1554354 to the University of Maryland. We appreciate the valuable suggestions, comments, and corrections from anonymous reviewers.

### References

- 510 Bray, N. A., Wijffels, S. E., Chong, J. C., Fieux, M., Hautala, S., Meyers, G., and Morawitz, W. M. L.: Characteristics of the Indo-Pacific throughflow in the Eastern Indian Ocean, *Geophys. Res. Lett.*, 24, 2569–2572, 1997.
- Clark, C. O., Webster, P. J., and Cole, J. E.: Interdecadal variability of the relationship between the Indian Ocean zonal mode and East African coastal rainfall anomalies, *J Climate*, 16, 548–554. [https://doi.org/10.1175/1520-0442\(2003\)016<0548:IVOTRB>2.0.CO;2](https://doi.org/10.1175/1520-0442(2003)016<0548:IVOTRB>2.0.CO;2), 2003.
- 515 Codiga, D. L., Renourad, D. P., and Fincham, A.: Experiments on waves trapped over the continental slope and shelf in a continuously stratified rotating ocean, *J. Mar. Res.*, 57, 585–612. doi: 10.1357/002224099321549602, 1999.





- Ding, X., Bassinot, F., Guichard, F., and Fang, N. Q.: Indonesian throughflow and monsoon activity records in the Timor Sea since the last glacial maximum, *Mar. Micropaleontol.*, 101, 115–126. <http://dx.doi.org/10.1016/j.marmicro.2013.02.003>, 2013.
- 520 Drushka, K., Sprintall, J., Gille, S., and Brodjonegoro, I.: Vertical structure of Kelvin waves in the Indonesian throughflow exit passages, *J. Phys. Oceanogr.*, 40, 1965–1987. doi:10.1175/2010 JPO4380.1, 2010.
- Duan, Y., Liu, L., Han, G., Liu, H., Yu, W., Yang, G., Wang, H., Wang, H., Liu, Y., Zahid, and Waheed, H.: Anomalous behaviors of Wyrтки Jets in the equatorial Indian Ocean during 2013, *Sci. Rep.*, 6(29688), 1–7. doi: 10.1038/srep29688., 2016.
- 525 Emery, W.J., and Thomson, R. E.: *Data Analysis Methods in Physical Oceanography*, Elsevier, New York, 2001.
- Fang, G., Wang, Y., Wei, Z., Fang, Y., Qiao, F., and Hu, X.: Interocean circulation and heat and freshwater budgets of the South China Sea based on numerical model, *Dynam. Atmos. Ocean*, 47(1-3), 55–72. <https://doi.org/10.1016/j.dynatmoce.2008.09.003>, 2009.
- Feng, M., and Wijffels, S.: Intraseasonal variability in the South Equatorial Current of the East Indian Ocean, *J. Phys. Oceanogr.*, 32, 265–277. [https://doi.org/10.1175/1520-0485\(2002\)032<0265:IVITSE>2.0.CO;2](https://doi.org/10.1175/1520-0485(2002)032<0265:IVITSE>2.0.CO;2), 2002.
- 530 Feng, M., Zhang, N., Liu, Q., and Wijffels, S.: The Indonesian throughflow, its variability and centennial change, *Geosci. Lett.*, 5(3), 1 – 10. <https://doi.org/10.1186/s40562-018-0102-2>, 2018.
- Ffield, A., Vranes, K., Gordon, A. L., Susanto, R. D., and Garzoli, S. L.: Temperature variability within Makassar Strait, *Geophys. Res. Lett.*, 27, 237–240. doi: 10.1029/1999GL002377, 2000.
- 535 Fieux, M., Andrie, C., Delecluse, P., Ilahude, A. G., Kartavtseff, A., Mantsi, F., Molcard, R., and Swallow, J. C.: Measurements within the Pacific-Indian Ocean throughflow region, *Deep-Sea Res.*, 41(7), 1091–1130. [https://doi.org/10.1016/0967-0637\(94\)90020-5](https://doi.org/10.1016/0967-0637(94)90020-5), 1994.
- Fieux, M., Molcard, R., and Ilahude, A. G.: Geostrophic transport of the Pacific-Indian Oceans throughflow, *J. Geophys. Res.*, 101(C5), 12,421–12,432. doi: 10.1029/95JC03566, 1996.
- 540 Gordon, A. L.: Interocean exchange of thermocline water, *J. Geophys. Res.*, 91, 5037–5046. doi: 10.1029/JC091iC04p05037, 1986.
- Gordon, A. L., and Susanto, R. D.: Makassar Strait transport: initial estimate based on Arlindo result, *Mar. Technol. Soc. J.*, 32, 34–45, 1999
- Gordon, A. L., Susanto, R. D., Ffield, A., Huber, B. A., Pranowo, W., and Wirasantosa, S.: Makassar Strait throughflow, 2004  
545 to 2006, *Geophys. Res. Lett.*, 35, L24605, 1–5. <https://doi.org/10.1029/2008HL036372>, 2008.
- Hallock, Z. R., Teague, W. J., and Jarosz, E.: Subinertial slope trapped waves in the northeastern Gulf of Mexico, *J. Phys. Oceanogr.*, 39, 1474–1485. doi:10.1175/2009JPO3925.1, 2009.
- Han, W., McCreary Jr, J. P., Anderson, D. L. T., and Mariano A. J.: Dynamics of the eastern surface jets in the equatorial Indian Ocean, *J. Phys. Oceanogr.*, 29(9), 2191–2209. doi: 10.1175/1520-0485(1999)029<2191:DOTESJ>2.0.CO;2,  
550 1999.



- Hannachi, A.: A Primer for EOF Analysis of Climate Data, Department of Meteorology, University of Reading. UK, 2004.
- Hanifah, F., and Ningsih, N. S.: The characteristic of eddies in the Banda Sea, *Adv Appl. Fluid Mech.*, 19(4), 889-902. ISSN: 0973-4686. <https://doi.org/10.17654/FM019040889>, 2016.
- 555 Huang, N. E., Shen, Z., Long, S. R., Wu, M. C., Shih, H. H., Zheng, Q., Yen, N-C., Tung, C. C., and Liu, H. H.: The empirical mode decomposition and the Hilbert spectrum for nonlinear and non-stationary time series analysis, *Roy. Soc.*, 454, 903–905. doi: 10.1098/rspa.1998.0193, 1998.
- Iskandar, I., Mardiansyah, W., Masumoto, Y., and Yamagata, T.: Intraseasonal Kelvin waves along the southern coast of Sumatra and Java, *J. Geophys. Res.*, 110, C04013. 1–12. doi:10.1029/2004JC002508, 2005.
- Iskandar, I., Tozuka, T., Sasaki, H., Masumoto, Y., and Yamagata, T.: Intraseasonal variations of surface and subsurface  
560 currents off Java as simulated in a high-resolution ocean general circulation model, *J. Geophys. Res.*, 111, C12015. 1–15. <https://doi.org/10.1029/2006JC003486>, 2006.
- Iskandar, I., Masumoto, Y., and Mizuno, K.: Subsurface equatorial zonal current in the eastern Indian Ocean, *J. Geophys. Res.*, 114, C06005. doi: doi:10.1029/2008JC005188, 2009.
- Kantha, L. H., and Clayson, C. A.: Numerical Models of Oceans and Oceanic Processes, International Geophysics Series. 66.  
565 Academic Press, London, 2000.
- Knox, R. A.: On a long series of measurements of Indian Ocean equatorial currents near Addu Atoll, *Deep-Sea Res.*, 23, 211–221. [https://doi.org/10.1016/0011-7471\(76\)91325-5](https://doi.org/10.1016/0011-7471(76)91325-5), 1976.
- Krishnamurthy, L., and Krishnamurthy, V.: Decadal and interannual variability of the Indian Ocean SST, *Clim. Dyn.*, 46(1–2), 57–70. <https://doi.org/10.1007/s00382-015-2568-3>, 2016.
- 570 Liu, Q, Feng, M., Wang, D., and Wijffels, S.: Interannual variability of the Indonesian Throughflow transport: a revisit based on 30-year expendable bathythermograph data, *J. Geophys. Res.*, 120, 8270 – 8282. doi:10.1002/2015JC011351, 2015.
- McPhaden, M. J.: Variability in the central equatorial Indian Ocean. Part I: Ocean dynamics, *J. Mar. Res.*, 40, 157–176, 1982.
- McPhaden, M. J., Wang, Y, and Ravichandran, M.: Volume transports of the Wyrki Jets and their relationship to the Indian Ocean dipole, *J. Geophys. Res.*, 120, 5302–5317. doi: 10.1002/2015JC010901, 2015.
- 575 Meng, X., Wu, D., Hu, R., and Lan, J.: The interdecadal variation of Indonesian throughflow and its mechanism, *Chinese Sci Bull.*, 49(19), 2058–2067. doi: 10.1360/03wd0540, 2004.
- Metzger, E. J., Hurlburt, H. E, Xu, X., Shriver, J. F., Gordon, A. L., Sprintall, J., Susanto, R. D., and (van) Aken, H. M.: Simulated and observed circulation in the Indonesian Seas 1/12° global HYCOM and the INSTANT Observation, *Dynam. Atmos. Ocean.*, 50, 275–300. <https://doi.org/10.1016/j.dynatmoce.2010.04.002>, 2010.
- 580 Meyers, G.: Variation of Indonesian throughflow and the El Niño Southern Oscillation, *J. Geophys. Res.*, 101, 12,255–12,263. doi: 10.1029/95JC03729, 1996.
- Murray, S. P., and Arief, D.: Throughflow into the Indian Ocean through the Lombok Strait, January 1985-January 1986, *Nat.*, 333, 444–447, 1988.



- Potemra, J. T.: Seasonal variations of upper ocean transport from the Pacific to the Indian Ocean via Indonesian straits, *J. Phys. Oceanogr.*, 29(11), 2930–2944. [https://doi.org/10.1175/1520-0485\(1999\)029<2930:SVOUOT>2.0.CO;2](https://doi.org/10.1175/1520-0485(1999)029<2930:SVOUOT>2.0.CO;2), 1999.
- 585 Pujiana, K., Gordon, A. L., and Sprintall, J.: Intraseasonal Kelvin wave in Makassar Strait, *J. Geophys. Res.*, 40, 2023–2034. doi: 10.1002/jgrc.20069., 2013.
- Pujiana, K., McPhaden, M. J., Gordon, A. L., and Napitu, A.: Unprecedented response of Indonesian Throughflow to anomalous Indo-Pacific climatic forcing in 2016, *J. Geophys. Res. Ocean.*, 124, 3737–3754. <https://doi.org/10.1029/2018JC014574>, 2019.
- 590 Qiu, Y., Li, L., and Yu, W.: Behavior of the Wyrтки Jet observed with surface drifting buoys and satellite altimeter, *Geophys. Res. Lett.*, 36(18), 120–131. doi: 10.1029/2009GL039120, 2009.
- Qu, T., and Meyers, G.: Seasonal characteristics of circulation in the southeastern tropical Indian Ocean, *J. Phys. Oceanogr.*, 35(2), 255–267. <https://doi.org/10.1175/JPO-2682.1>, 2005.
- 595 Quadfasel D., and Cresswell, G. R.: A note on seasonal variability of the South Java Current, *J. Geophys. Res.*, 97(C3), 3685–3688. <https://doi.org/10.1029/91JC03056>, 1992.
- Saji N. H., Goswami, B. N., Vinayachandran, P. N., and Yamagata, T.: A dipole mode in the tropical Indian Ocean, *Nat.*, 401, 360–363. doi: 10.1038/43854, 1999.
- Saji, N. H., and Yamagata, T.: Possible impacts of Indian Ocean dipole mode events on global climate, *Clim. Res.*, 25(2), 151–169. doi: 10.3354/cr025151, 2003.
- 600 Semtner, A. J., and Chervin, R. M.: Ocean general circulation from a global eddy-resolving model, *J. Geophys. Res.*, 97, 5493–5550. <https://doi.org/10.1029/92JC00095>, 1992.
- Shen, B., heung, S., Wu, Y., Li, J. F., and Kao, D.: Parallel implementation of the ensemble empirical mode decomposition and its application for earth science data analysis, *Comput. Sci. Eng.*, 19(5), 49–57. <https://doi.org/10.1109/MCSE.2017.3421555>, 2017.
- 605 Shinoda, T., Han, W., Metzger, E. J., and Hurlburt, H.: Seasonal variation of the Indonesian throughflow in Makassar Strait, *J. Phys. Oceanogr.*, 42, 1099–1123. <https://doi.org/10.1175/JPO-D-11-0120.1>, 2012.
- Song, Q., Gordon, A. L., and Visbeck, M.: Spreading of the Indonesian throughflow in the Indian Ocean, *J. Phys. Oceanogr.*, 34, 772–792. [https://doi.org/10.1175/1520-0485\(2004\)034<0772:SOTITI>2.0.CO;2](https://doi.org/10.1175/1520-0485(2004)034<0772:SOTITI>2.0.CO;2), 2004.
- 610 Sprintall, J., Chong, J., Syamsudin, F., Morawitz, W., Hautala, S., Bray, N., and Wijffels, S.: Dynamics of the South Java Current in the Indo-Australian basin, *Geophys. Res. Lett.*, 26(16), 2493–2496. <https://doi.org/10.1029/1999GL002320>, 1999.
- Sprintall, J., Gordon, A. L., Murtugudde, R., and Susanto, R. D.: A semi-annual Indian Ocean forced Kelvin waves observed in the Indonesian Seas, May 1997, *J. Geophys. Res.*, 105, 17. 217–17. 230. <https://doi.org/10.1029/2000JC900065>, 2000.
- 615 Sprintall, J., Wijffels, S. E., Molcard, R., Jaya, I.: Direct estimates of the Indonesian throughflow entering the Indian Ocean: 2004–2006, *J. Geophys. Res.*, 114, C07001. 1–19. doi: 10.1029/2008JC005257, 2009.



- Sprintall, J., Wijffels, S. E., Molcard, R., and Jaya, I.: Direct evidence of the south Java current in Ombai Strait, *Dynam. Atmos. Ocean.*, 50, 140–156. <https://doi.org/10.1016/j.dynatmoce.2010.02.006>, 2010.
- 620 Sprintall, J., and Révelard, J.: The Indonesian throughflow response to Indo-Pacific climate variability, *J. Geophys. Res. Ocean.*, 119, 1161–1175. doi: 10.1002/2013JC009533, 2014.
- Susanto, R. D., Gordon, A. L., Sprintall, J., and Herunadi, B.: Intraseasonal variability and tides in Makassar Strait, *Geophys. Res. Lett.*, 27(10), 1499–1502. <https://doi.org/10.1029/2000GL011414>, 2000.
- Susanto, R. D., Gordon, A. L., and Zheng, Q.: Upwelling along the coasts of Java and Sumatra and its relation to ENSO, *Geophys. Res. Lett.*, 28(8), 1599–1602. <https://doi.org/10.1029/2000GL011844>, 2001.
- 625 Susanto, R. D., and Gordon, A. L.: Velocity and transport of the Makassar Strait throughflow, *J. Geophys. Res.*, 110, C01005. 1–10. <https://doi.org/10.1029/2004JC002425>, 2005.
- Susanto, R. D., Ffield, A., Gordon, A. L., and Adi, T. R.: Variability of Indonesian throughflow within Makassar Strait, 2004–2009, *J. Geophys. Res.*, 117, C09013. 1–16. doi: 10.1029/2012JC008096, 2012.
- 630 Susanto, R. D., and Song, Y. T.: Indonesian throughflow proxy from satellite altimeters and gravimeters, *J. Geophys. Res., Ocean.* 120, 2844–2855. doi:10.1002/2014JC010382, 2015.
- Susanto, R. D., Wei, Z., Adi, T. R., Zheng, Q., Fang, G., Bin, F., Supangat, A., Agustadi, T., Li, S., Trenggono, and M., Setiawan, A.: Oceanography surrounding Krakatau Volcano in the Sunda Strait, Indonesia, *Oceanography*, 29(2), 228–237. <https://doi.org/10.5670/oceanog.2016.31>, 2016.
- 635 Syamsudin, F., Kaneko, A., and Haidvogel, D. B.: Numerical and observational estimates of Indian Ocean Kelvin wave intrusion into Lombok Strait, *Geophys. Res. Lett.*, 31, L24307. 1–4. doi:10.1029/2004GL021227, 2004.
- Syamsudin, F., and Kaneko, A.: Ocean variability along the southern coast of Java and Lesser Sunda Islands, *J. Oceanogr.*, 69(5), 557–570. <https://doi.org/10.007/s10872-013-0192-6>, 2013.
- Tomczak, M., and Godfrey, J. S.: *Regional Oceanography: An Introduction*, Pergamon Press, Oxford, 1994.
- 640 Wijffels, S., Sprintall, J., Fieux, M., and Bray, N.: The JADE and WOCE I10/IR6 throughflow sections in the southeast Indian Ocean. Part 1: water mass distribution and variability, *Deep-Sea Res. PT II.*, 49, 1341–1362. [https://doi.org/10.1016/S0967-0645\(01\)00155-2](https://doi.org/10.1016/S0967-0645(01)00155-2), 2002.
- Wijffels, S., and Meyers, G.: An intersection of oceanic waveguides: variability in the Indonesian throughflow region, *J. Phys. Oceanogr.*, 34, 1232–1253. [https://doi.org/10.1175/1520-0485\(2004\)034<1232:AIOOWV>2.0.CO;2](https://doi.org/10.1175/1520-0485(2004)034<1232:AIOOWV>2.0.CO;2), 2004.
- 645 Wu, Z., and Huang, N. E.: Ensemble empirical mode decomposition: a noise-assisted data analysis method, *Adv. Adapt. Data Anal.*, 1, 1–41. doi: 10.1142/S1793536909000047, 2009.
- Wyrтки, K.: An equatorial jet in the Indian Ocean, *Sci.*, 181, 262–264, 1973.
- Wyrтки, K.: Indonesian throughflow and the associated pressure gradient, *J. Geophys. Res.*, 92, 12,941–12,946, 1987.
- Yamagami, Y., and Tozuka, T.: Interannual variability of South Equatorial Current bifurcation and western boundary currents  
650 along the Madagascar coast, *J. Geophys. Res. Ocean.*, 120, 8551–8570. doi: 10.1002/2015JC011069, 2015.



Yuan, Y., Chan, C. L. J., Wen, Z., and Chongyin, L.: Decadal and interannual variability of the Indian Ocean dipole, Adv. Atmos. Sci., 25(5), 856–866. doi: 10.1007/s00376-008-0856-0, 2008.

Zhang, N., Feng, M., Du, Y., Lan, J. and Wijffels, S. E.: Seasonal and interannual variations of mixed layer salinity in the southeast tropical Indian Ocean, J. Geophys. Res., Ocean. 121, 4716 – 4731. doi:10.1002/2016JC011854, 2016.

655

**Table 1. Correlation coefficients between zonal currents at 100 m depth at both  $A_{WJ}$  and  $A_{EJ}$  and each the local NW zonal wind and subsurface (200 m) maximum ITF in the southern Ombai Strait during DJF in the period of 2004 through 2006.**

Points	Correlation Coefficients ( $r$ ) <sup>a)</sup>	
	$U$ -SMITF	$U$ -NWZW
$A_{WJ}$	0.76	-0.32 <sup>b)</sup>
$A_{EJ}$	-0.13 <sup>b)</sup>	0.30 <sup>b)</sup>

<sup>a)</sup> The 95% significance level is approximately  $\pm 0.33$ .  $U$ : zonal currents at 100 m depth; SMITF: subsurface (200 m) maximum ITF in the southern Ombai Strait; NWZW: northwesterly zonal wind.

660 <sup>b)</sup> Correlation below the significance level.

**Table 2. Dominant variances at the nine observation points.**

Mode	Variance (%)								
	$A_{SM}$	$A_{WJ}$	$A_{EJ}$	$B_{SM}$	$B_{WJ}$	$B_{EJ}$	$C_{SM}$	$C_{WJ}$	$C_{EJ}$
1	37	<b>58</b>	60	<b>64</b>	84	76	88	87	<b>72</b>
2	25	33	29	27	12	18	9	10	20
3	13	5	6	6		4			3
4	10								2
5	6								
6	4								
<b>Total</b>	<b>95</b>	<b>96</b>	<b>95</b>	<b>97</b>	<b>96</b>	<b>98</b>	<b>97</b>	<b>97</b>	<b>97</b>

**Table 3. Maximum energy density at intraseasonal, semiannual, annual, and interannual timescales at points  $A_{WJ}$ ,  $B_{SM}$ , and  $C_{EJ}$ .**

Points	Maximum Energy Density (Power/Year)			
	IS	SA	AN	IA
$A_{WJ}$	0.070	0.140	0.038	0.003
$B_{SM}$	0.033	0.135	0.007	0.012
$C_{EJ}$	0.012	0.008	0.012	0.017

665 IS: Intraseasonal; SA: Semiannual; AN: Annual; IA: Interannual.



**Table 4. Lag correlation between the zonal currents at 30 m and each the ONI and DMI.**

Points	Correlation Coefficients ( $r$ ) <sup>a)</sup> and Time Lag (TL)			
	ONI - $U$		DMI - $U$	
	$r$	TL (months)	$r$	TL (months)
A <sub>WJ</sub>	0.02 <sup>b)</sup>	2	-0.09	9
B <sub>SM</sub>	0.24	18	-0.28	1
C <sub>EJ</sub>	0.27	4	-0.13	11

<sup>a)</sup> The 95% significance level is approximately  $\pm 0.07$ .  $U$ : zonal currents at 30 m. Positive correlation coefficients between the currents and the ONI indicate existence of an eastward (westward) anomaly of the currents during El Niño (La Niña). Meanwhile, negative correlation coefficients between the currents and the DMI indicate existence of an eastward (westward) anomaly of the currents during negative (positive) IOD. A positive (negative) lag indicates that the variability in a former variable (e.g., ONI or DMI) leads (lags) that in the latter variable (the zonal current).

<sup>b)</sup> Correlation below the significance level.

**Table 5. ENSO, IOD, and neutral events during the 1950 – 2013 periods.**

	El Niño			NR-ENSO			La Niña		
<b>P-IOD</b>	1951	1953	1963	1962	1967	1990	1970	1976	1985
	1965	1966	1969	2003	2013		1999	2000	2006
	1972	1977	1982				2007	2008	2010
	1983	1986	1987				2011		
	1991	1993	1994						
	1997	2002	2004						
	2009	2012							
<b>NR-IOD</b>				1952	1957	1961	1950	1971	1973
				1979	2001	2005	1974	1988	1989
							1995		
<b>N-IOD</b>	1968	1992		1956	1958	1959	1954	1955	1964
				1960	1978	1980	1975	1984	1998
				1981	1996				

NR-ENSO: neutral ENSO ( $-0.5\text{ °C} < \text{ONI} < +0.5\text{ °C}$ ); El Niño ( $\text{ONI} > +0.5\text{ °C}$ ); La Niña ( $\text{ONI} < -0.5\text{ °C}$ ); P-IOD: Positive IOD ( $\text{DMI} > +0.36\text{ °C}$ ); NR-IOD: neutral IOD ( $-0.36\text{ °C} < \text{DMI} < +0.36\text{ °C}$ ); N-IOD: negative IOD ( $\text{DMI} < -0.36\text{ °C}$ ). The classification of ENSO events is determined by ONI (<http://www.ESRL.noaa.gov/>). Meanwhile, DMI is used for the classification of IOD events, with criterion according to Yuan et al. (2008).



**Table 6. Summary of major climate modes (ENSO and/or IOD) and the corresponding current anomalies through 1950 – 2013.**

Points	Events	Zonal Current ( $U$ )	
		Current Speed ( $\text{m s}^{-1}$ )	Observation Time
<b>B<sub>SM</sub></b>	NR-ENSO (Jan. 2004) and NR-IOD (Jun. 2005)	-0.21	Jul. 2005
	NR-ENSO (Dec 1980) and P-IOD (May 1982)	-0.19	Jun. 1982
	NR-ENSO (Aug. 1962) and N-IOD (Jan. 1964)	-0.28	Feb. 1964
	El Niño (Feb. 1998) and P-IOD (Jul. 1999)	-0.35	Aug. 1999
	El Niño (Oct. 2009) and P-IOD (Apr. 2011)	-0.18	May 2011
	La Niña (Dec. 1995) and P-IOD (Jul. 1997)	-0.50	Aug. 1997
	La Niña (Aug. 2007) and P-IOD (Feb. 2009)	-0.16	Mar. 2009
	La Niña (Feb. 1995) and N-IOD (Jul. 1956)	-0.24	Aug. 1956
<b>C<sub>EJ</sub></b>	La Niña (Oct. 1955) and NR-IOD (Mar. 1957)	-0.13	Apr. 1957
	NR-ENSO (Oct. 2001) and NR-IOD (Feb. 2001)	-0.18	Jan. 2002
	NR-ENSO (May. 1978) and P-IOD (Oct. 1977)	-0.46	Sep. 1978
	NR-ENSO (Mar. 1960) and N-IOD (Aug. 1959)	0.41	Jul. 1960
	El Niño (Aug. 1953) and P-IOD (Jan. 1953)	0.96	Dec. 1953
	El Niño (Nov. 1991) and P-IOD (Apr. 1991)	0.45	Mar. 1992
	El Niño (Nov. 2009) and P-IOD (Apr. 2009)	0.69	Jan. 2010
	El Niño (Jul. 1997) and N-IOD (Dec. 1996)	0.78	Nov. 1997
	La Niña (May. 1988) and P-IOD (Oct. 1987)	-0.46	Sep. 1988
	La Niña (Sep. 1998) and P-IOD (Feb. 1998)	-0.59	Jan. 1999
	La Niña (Nov. 2011) and P-IOD (Apr. 2011)	-0.61	Mar. 2012
	La Niña (Aug. 1954) and NR-IOD (Jan. 1954)	-0.70	Dec. 1954
La Niña (Sep. 1988) and NR-IOD (Feb. 1988)	-0.43	Jan. 1989	

NR-ENSO: neutral ENSO; P-IOD: Positive IOD; NR-IOD: neutral IOD; N-IOD: negative IOD. The classification criterion for ENSO and IOD events can be seen in Table 5.

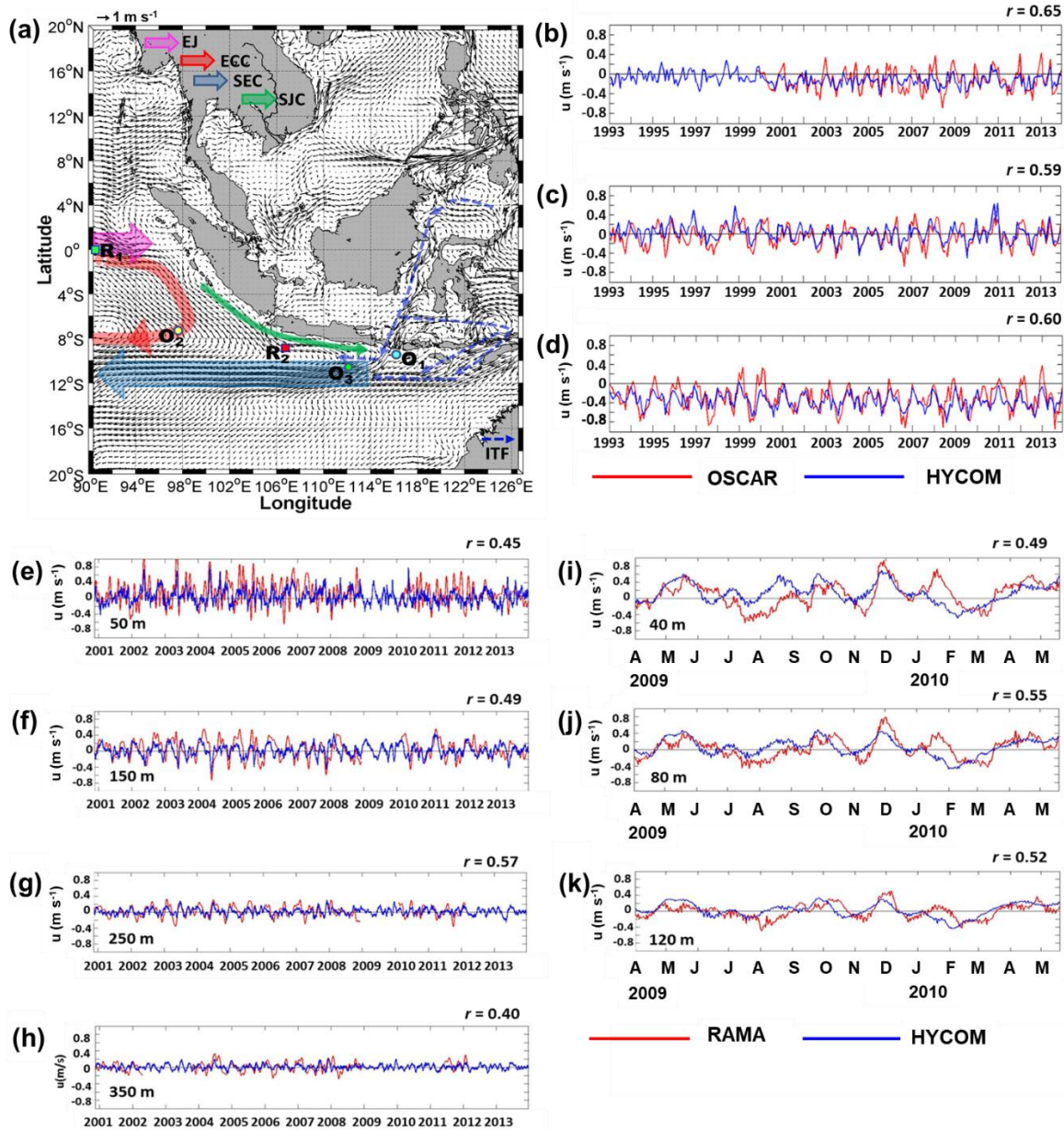
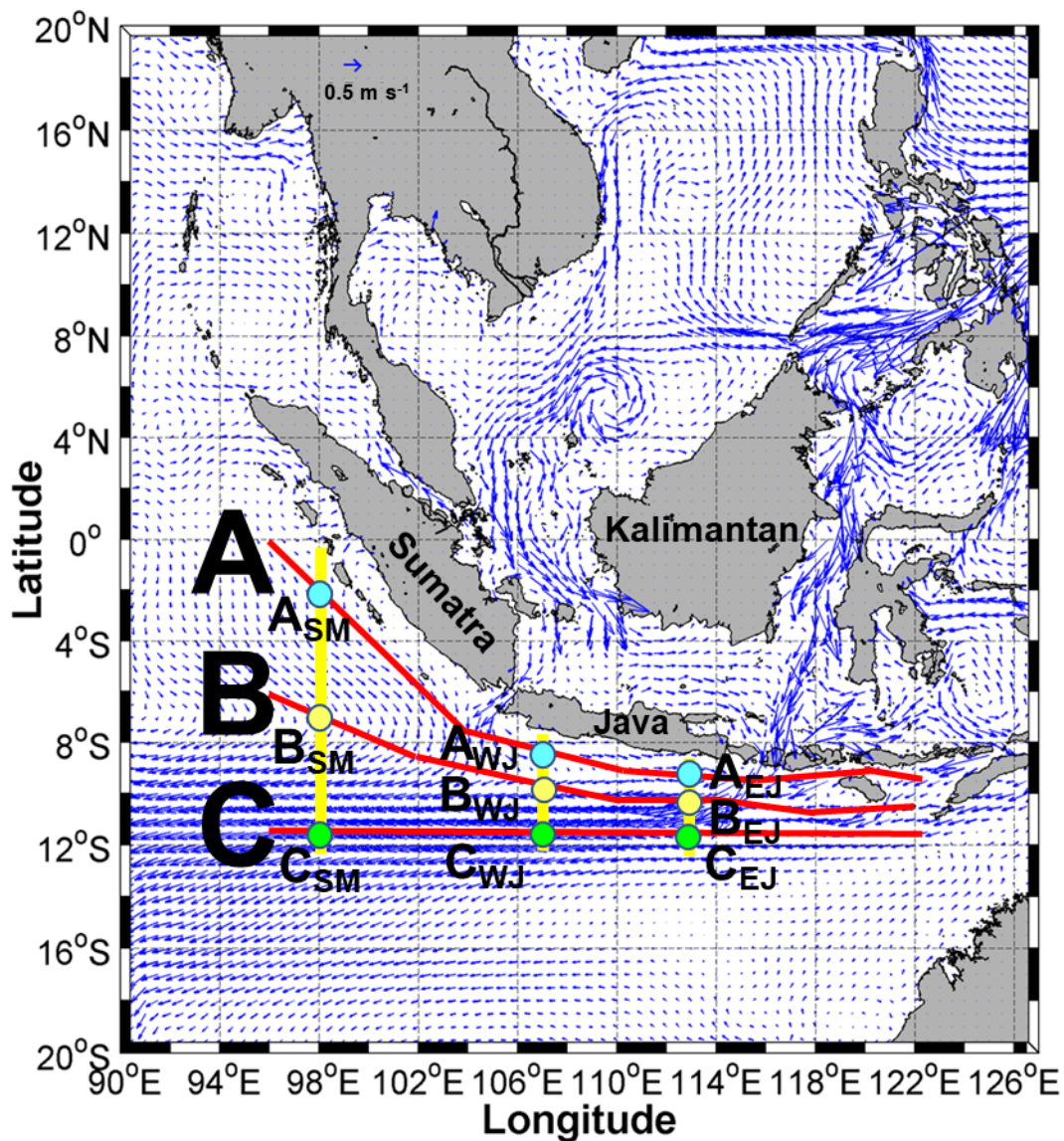


**Figure 1.** Validation of HYCOM zonal currents with OSCAR and RAMA datasets: (a) Locations of validation points: Points O<sub>1</sub> (8°S, 116°E), O<sub>2</sub> (7°S, 98°E), and O<sub>3</sub> (11.5°S, 113°E) for the OSCAR data, while R<sub>1</sub> (0°S, 90°E) and R<sub>2</sub> (8.5°S, 106.75°E) for the RAMA data. (b)-(d) Time series of the zonal currents observed by the HYCOM (blue lines) and the OSCAR (red lines) at a depth of 0.5 m at point O<sub>1</sub>, O<sub>2</sub>, and O<sub>3</sub>, respectively. Meanwhile (e)-(h) are the time series of zonal currents observed by the HYCOM (blue lines) and the moored RAMA (red lines) at point R<sub>1</sub> at depths of 50, 150, 250, and 350 m, sequentially. Meanwhile, (i)-(k) are the same as (e)-(h), except for point R<sub>2</sub> and depths of 40, 80, and 120 m, respectively. In the Figures 1e-h (point R<sub>1</sub>), a monthly low-pass filter has been applied before plotting.

690





695 **Figure 2.** The area of study interest in the SETIO region adjacent to the Sumatra-Java southern coasts. The blue arrows show  
climatological (yearly mean) surface (1 m) current field over 64 years from 1950 to 2013. Yellow lines are the meridional  
sections along the three longitudes (98°E, 107°E, and 113°E), while red lines are the three selected transects: A, B, and C.  
Green, yellow, and cyan circles are the locations in which the zonal currents are analysed, namely points  $A_{SM}$ ,  $A_{WJ}$ ,  $A_{EJ}$   
(on the Transect A); points  $B_{SM}$ ,  $B_{WJ}$ , and  $B_{EJ}$  (on the Transect B); and points  $C_{SM}$ ,  $C_{WJ}$ , and  $C_{EJ}$  (on the Transect C). The  
subscripts SM, WJ, and EJ denote regions which close to Sumatra, West Java, and East Java.

700

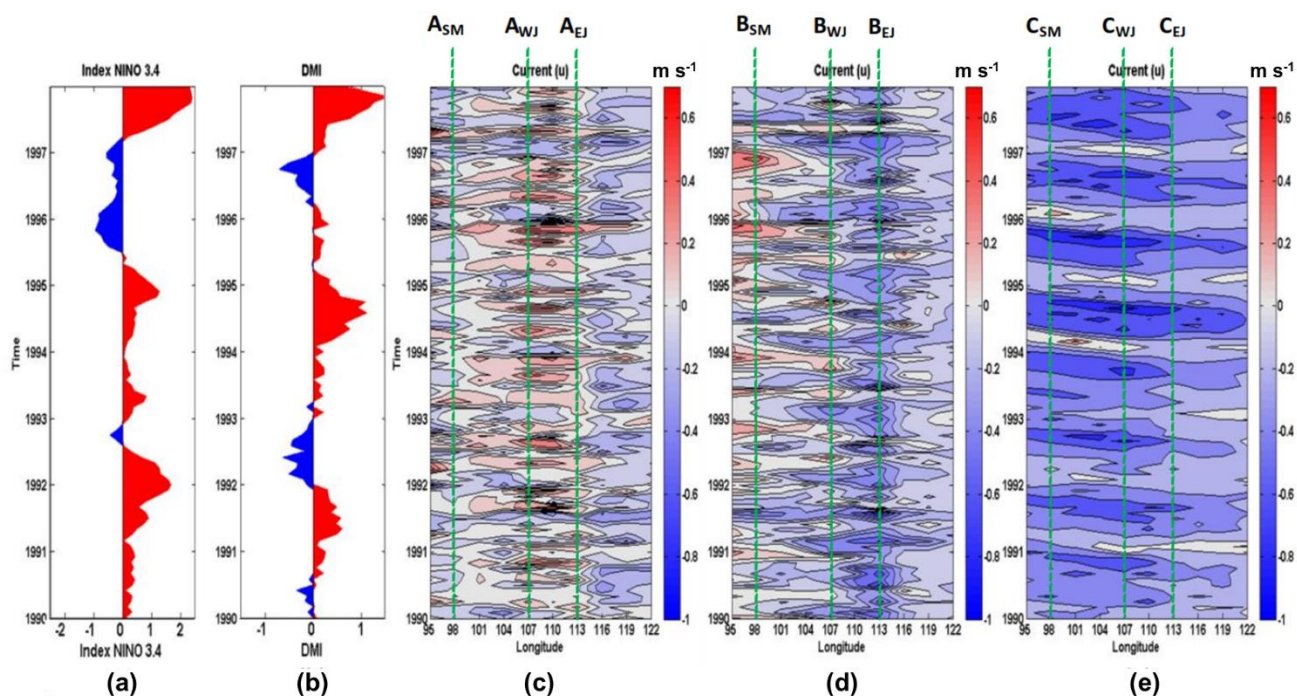
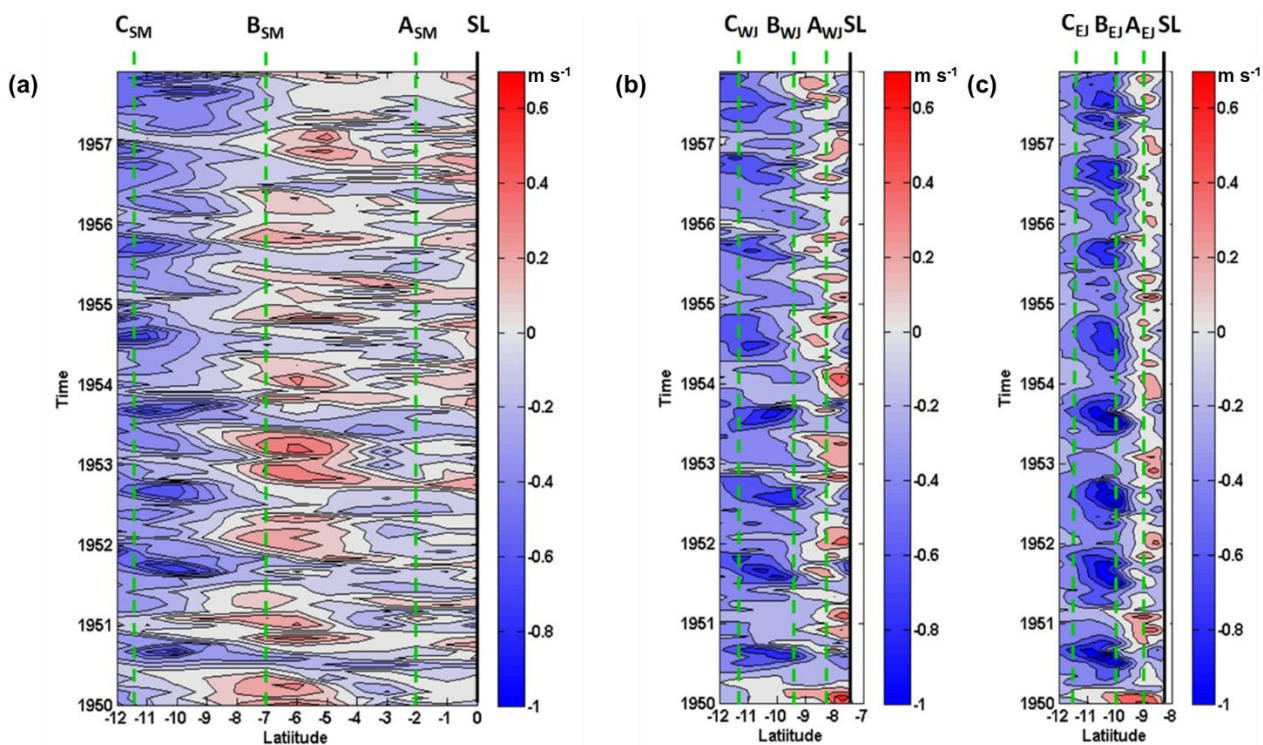
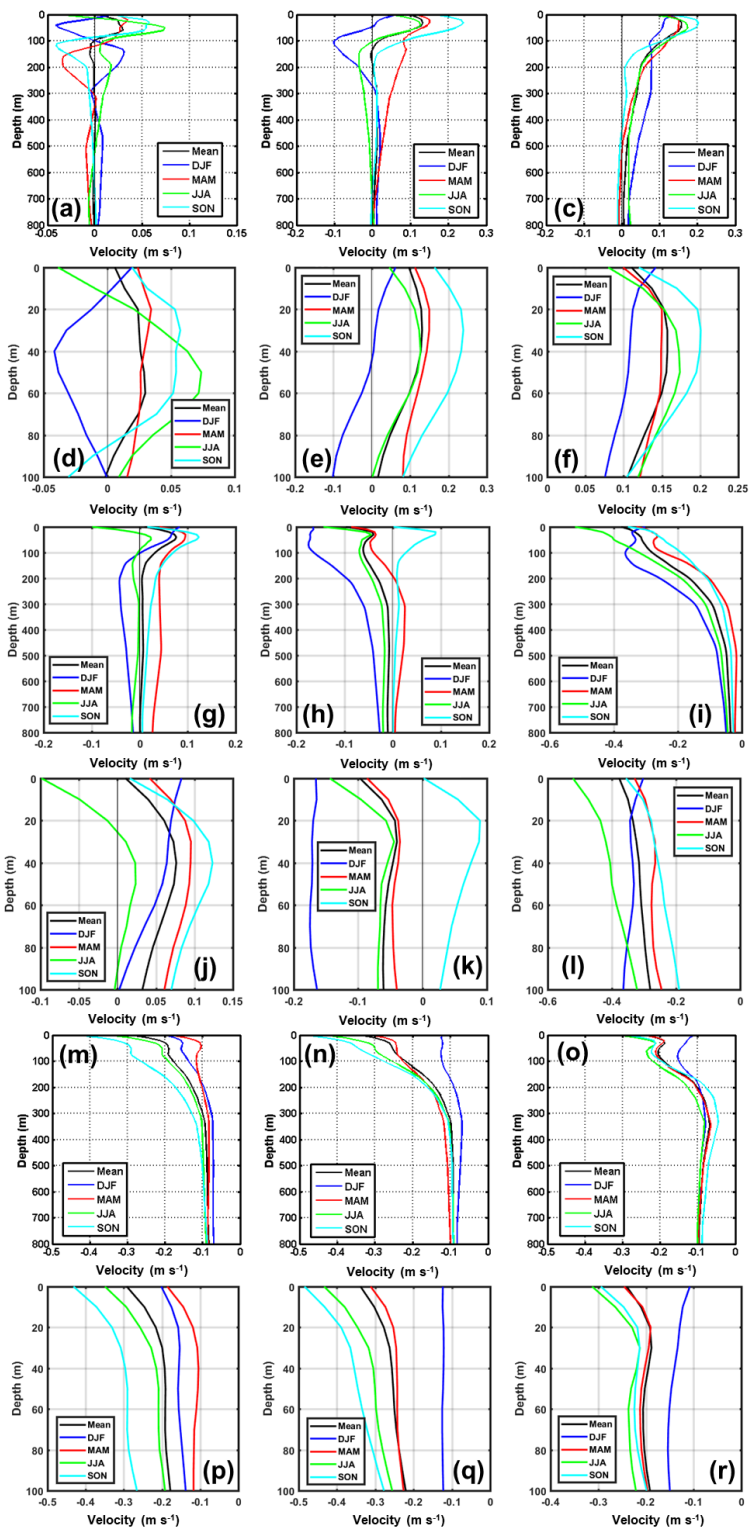


Figure 3. Time-longitude profiles of: (a) the ONI, (b) the DMI; and monthly averages of surface (1 m) zonal currents along (c) Transect A, (d) Transect B, and (e) Transect C. Positive (negative) values of the zonal currents indicate eastward (westward). Meanwhile, green dash lines denote longitudes of the nine selected points.

705



**Figure 4.** The zonal surface (1 m) currents along three meridional sections (yellow lines in Figure 2): (a) 98°E, (b), 107°E, and (c) 113°E. Positive (negative) values of the zonal currents indicate eastward (westward). Meanwhile, green dash lines denote latitudes of the nine selected points and SL is shoreline.





**Figure 5.** Mean and seasonal depth profiles of zonal current velocity derived from the HYCOM simulation results for the period of 1950 through 2013, at points: (a) ASM, (b) AWJ, (c) AEI, (g) BSM, (h) BWJ, (i) BEJ, (m) CSM, (n) CWJ, and (o) CEJ. Meanwhile, (d)-(f), (j)-(l), and (p)-(r) are the same as (a)-(c), (g)-(i), and (m)-(o), respectively, except for depths of 0-100 m.

715

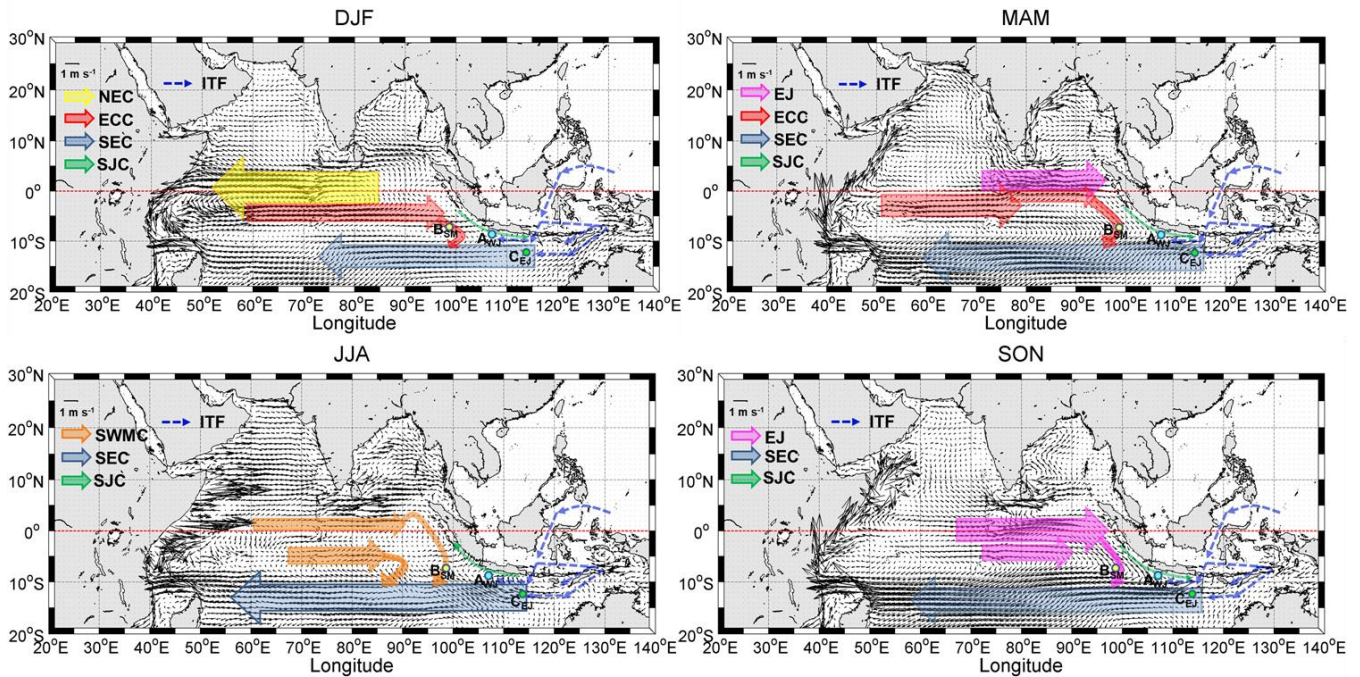


**Figure 6.** Seasonal averaged surface (1 m) currents over 64 years (1950-2013) and schematics of the tropical current systems in the Indian Ocean during (a) DJF, (b) MAM, (c) JJA, and (d) SON. Current branches indicated by colour arrows (not black) are the North Equatorial Current (NEC), Equatorial Counter Current (ECC), South Equatorial Current (SEC), South Java Current (SJC), Wyrтки Jet (WJ), South West Monsoon Current (SWMC), and Indonesian Throughflow (ITF). The dashed line represents thermocline current.

720

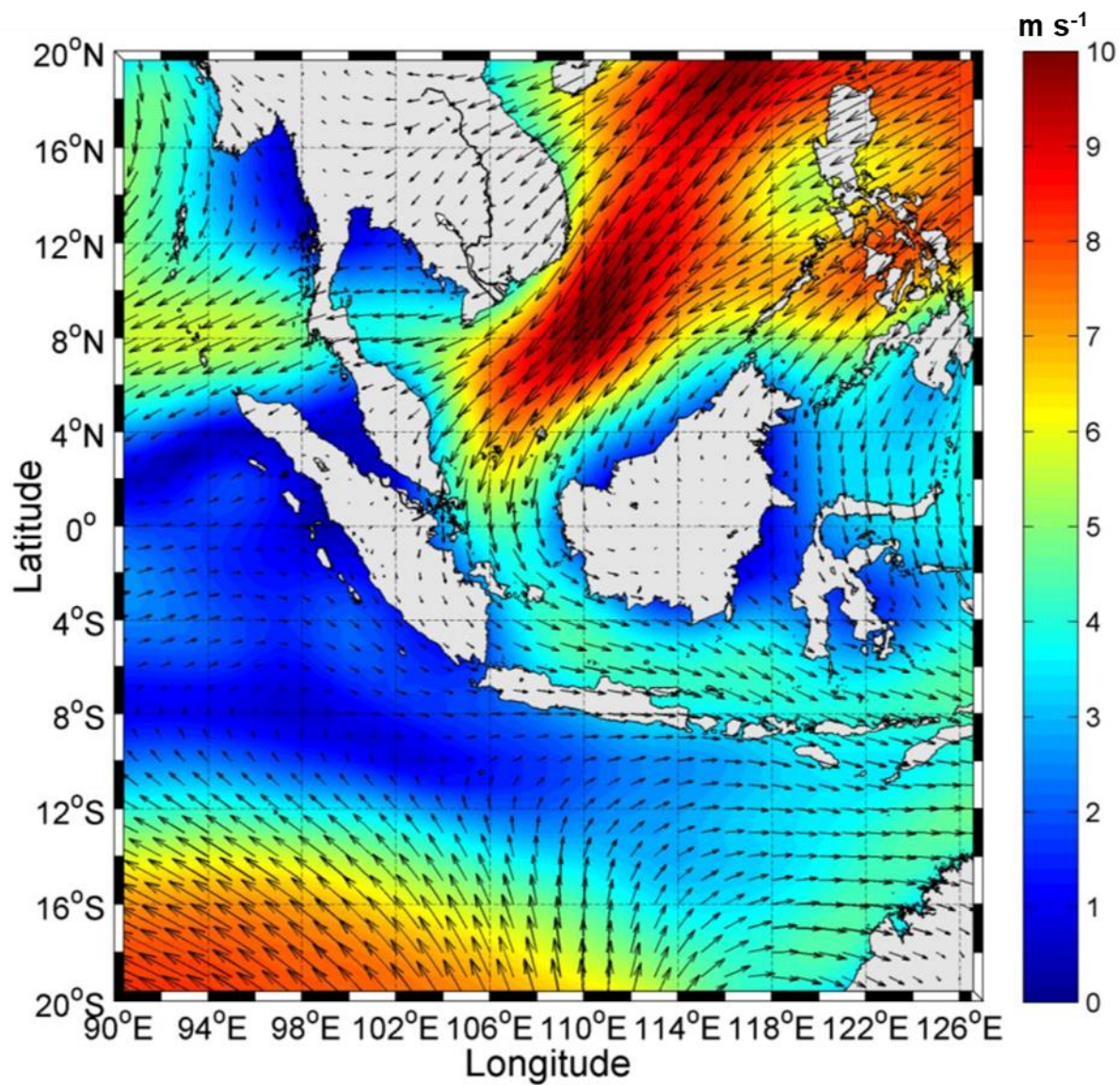
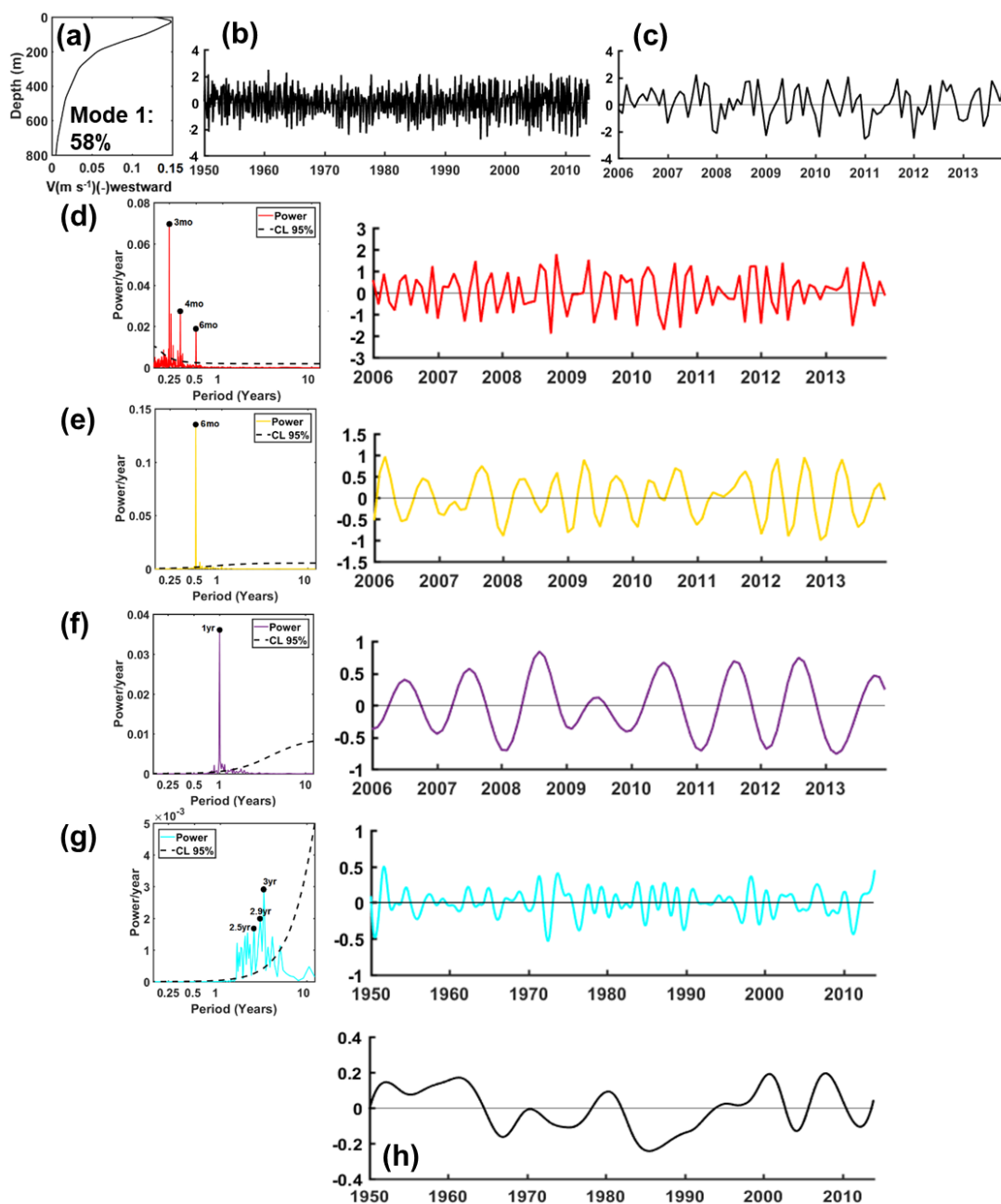


Figure 7. Mean NW monsoon for the period of 1950 to 2013 (climatological wind field during the DJF).



**Figure 8.** (a) Vertical structure and (b) its associated temporal variability of EOF1 (58% of total variance) at the point Awj. (c) As (b), except for the last eight-year period of the EOF1. The EEMD (i.e., Huang et al., 1998; Shen et al., 2017) is then applied to the EOF temporal structure to decompose temporal variability: (d) intraseasonal, (e) semiannual (f) annual, and (g) interannual variabilities with their corresponding red spectrum as a reference for 95% confidence limit (left panel), whereas (h) represents the long-term trend.

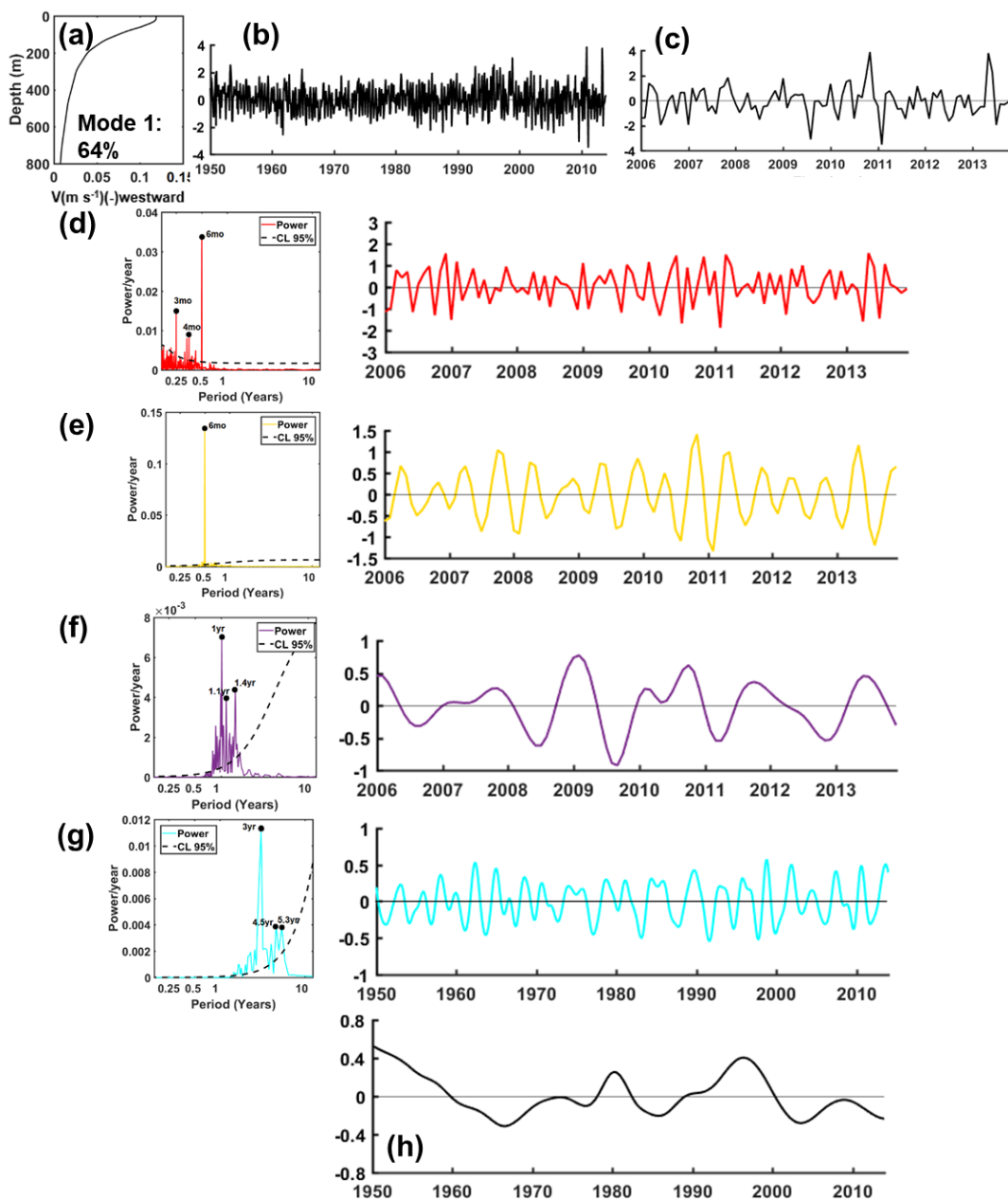


Figure 9. Same as in Figure 8, except for the point B<sub>SM</sub> with the temporal variability of EOF1 accounting for 64% of total variance.



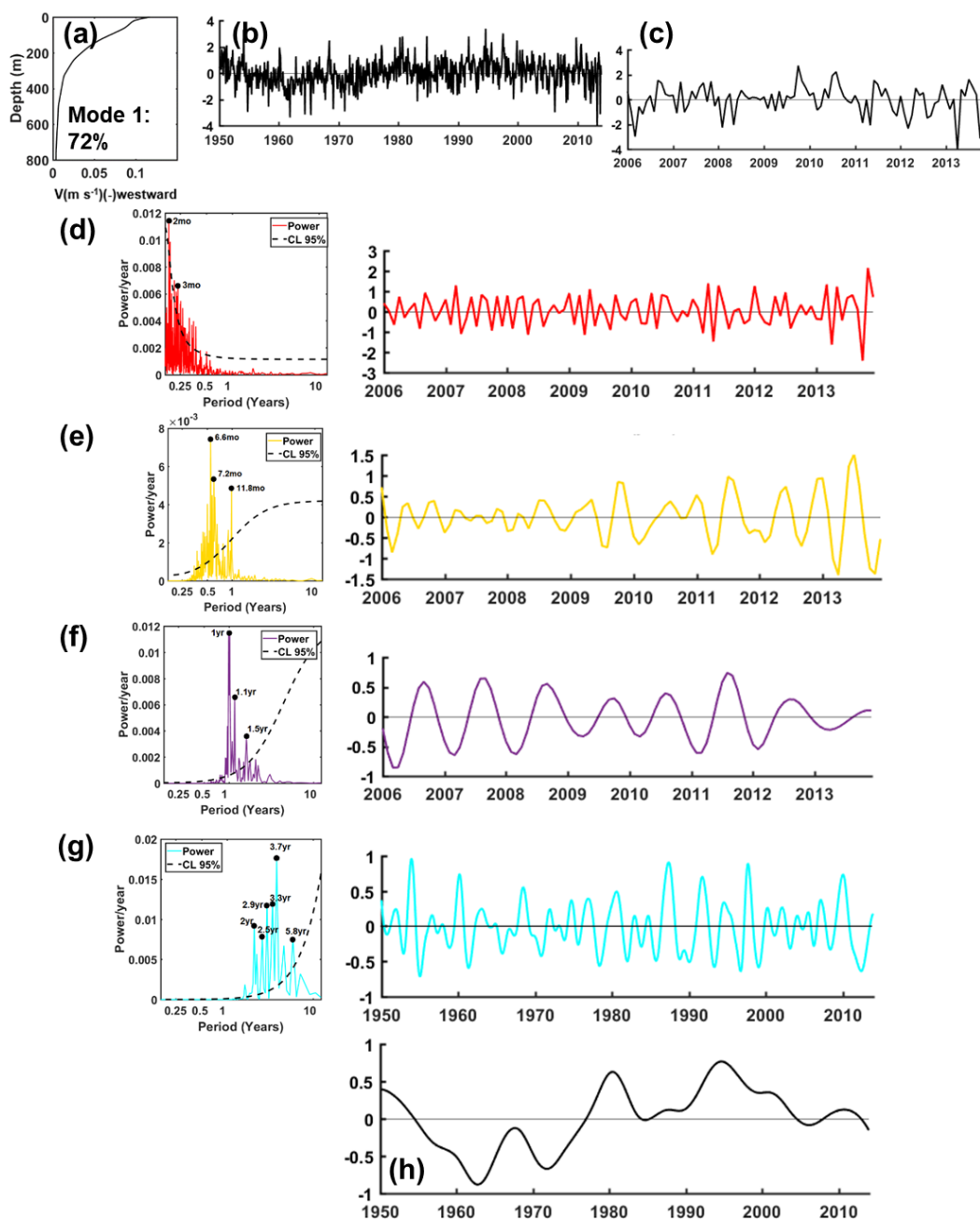
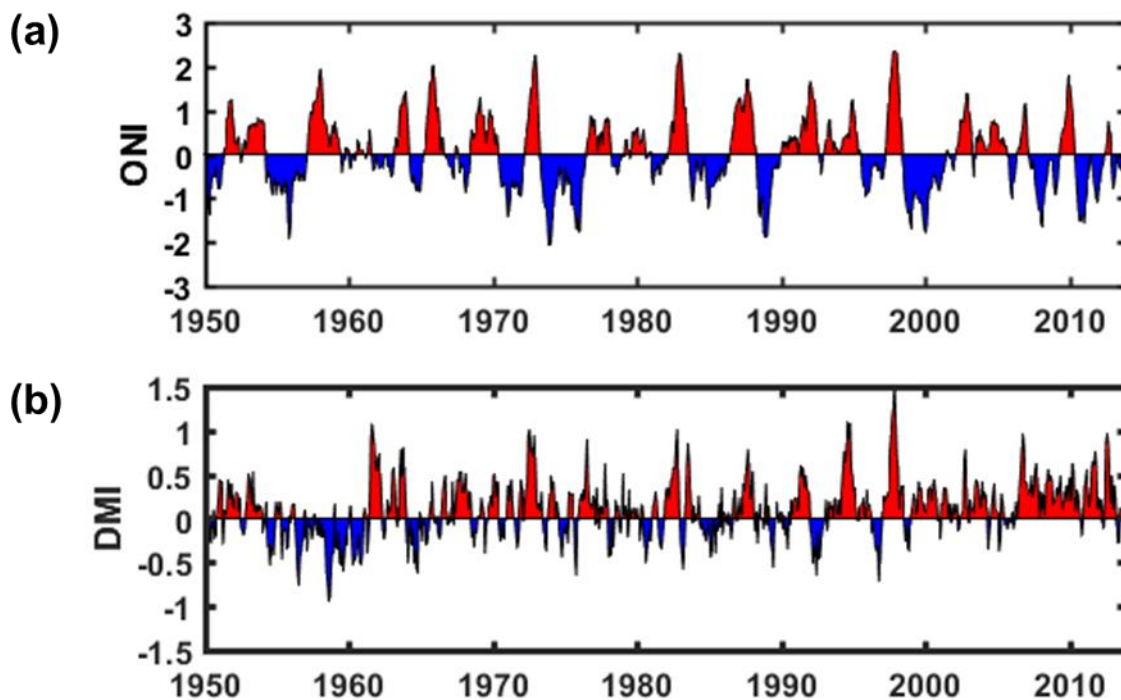


Figure 10. Same as in Figure 8, except for the point CEJ with the temporal variability of EOF1 accounting for 72% of total variance.



740 Figure 11. (a) ONI and (b) DMI indices from 1950 to 2013

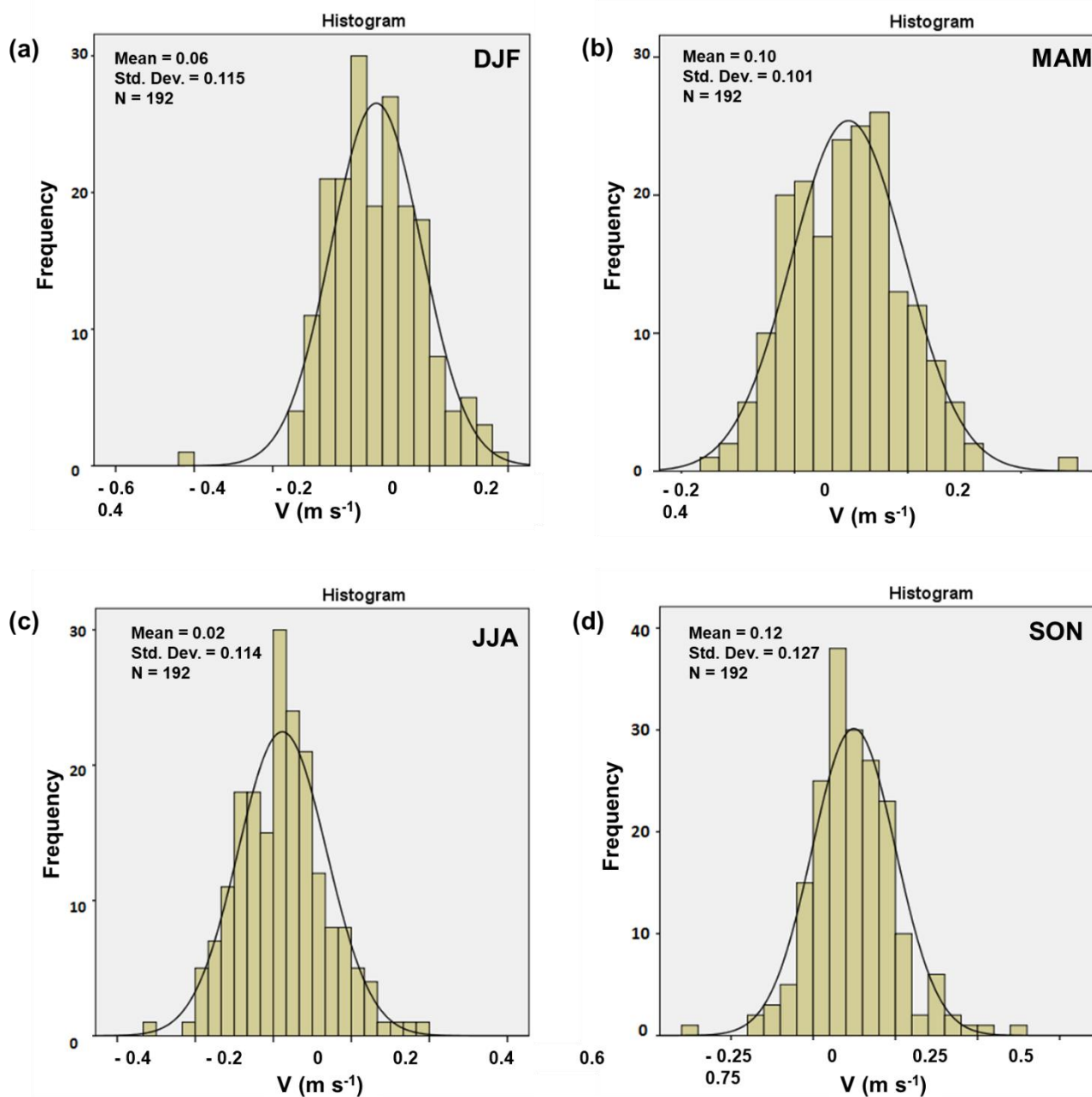


Figure 12. A probability distribution function of the EOF1 of zonal currents for each of the NW (a), SE (c), and transition (b and d) seasons at B<sub>SM</sub> at a depth of ~40 m.

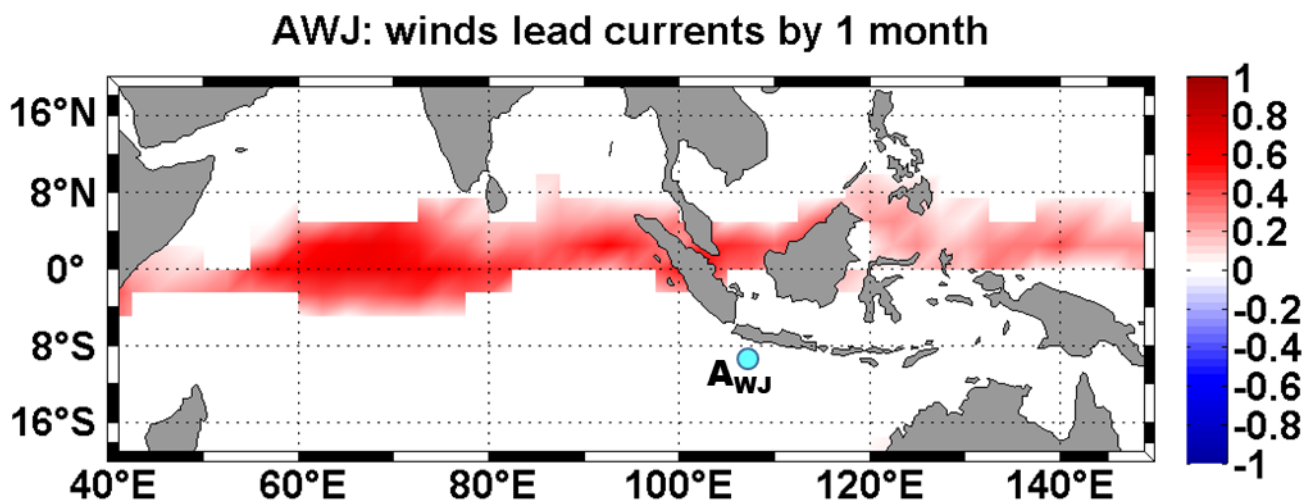
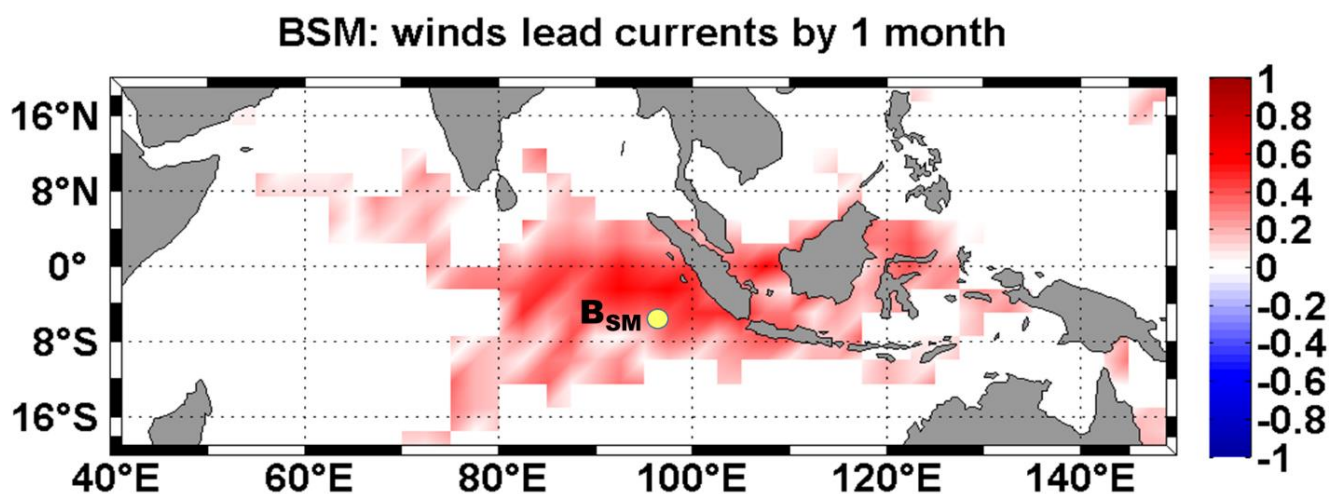
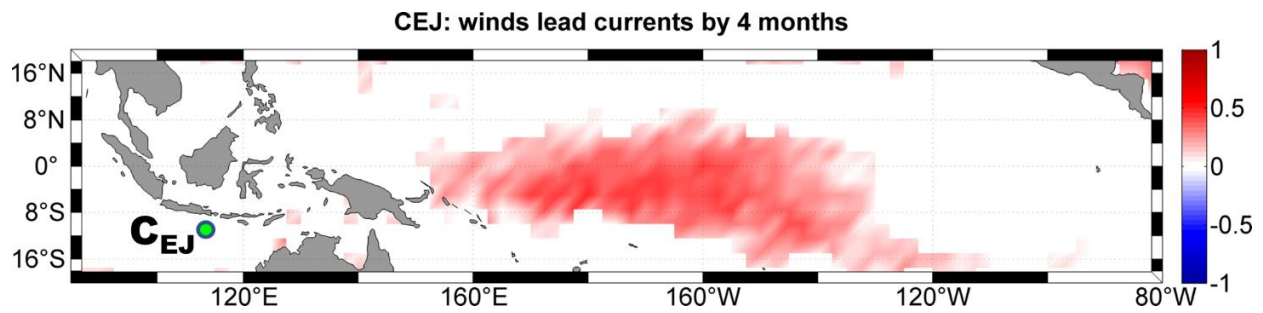


Figure 13. A correlation map between zonal wind and zonal currents (at 30 m) at  $A_{WJ}$  for the semiannual signals extracted using the EEMD method. The 99% significance level is approximately  $\pm 0.07$ .



750

Figure 14. As in Figure 13, but at  $B_{SM}$  and for interannual signal.



**Figure 15.** As in Figure 13, but at  $C_{EJ}$  and for interannual signal.

755